Master's thesis

NTNU
Norwegian University of Science and Technology
Faculty of Natural Sciences
Department of Materials Science and Engineering

Håvard Bærug

Field Dependent Conductivity of Cyclohexane

Master's thesis in Materials Science and Engineering
Supervisor: Julia Glaum
July 2020

NTNU
Norwegian University of
Science and Technology

Håvard Bærug

Field Dependent Conductivity of Cyclohexane

Master's thesis in Materials Science and Engineering
Supervisor: Julia Glaum
July 2020

Norwegian University of Science and Technology
Faculty of Natural Sciences
Department of Materials Science and Engineering

NTNU
Norwegian University of
Science and Technology

Preface

This project has been performed as a part of the course "TMT4905 Materials Technology, Master's Thesis" at Norwegian University of Science and Technology (NTNU), in cooperation with SINTEF Energy Research.

I would like thank all those who have contributed to this project. Julia Glaum (NTNU) has been the main supervisor of the project, with Øystein Hestad (SINTEF Energy Research) as co-supervisor, and both have offered plenty of insight and feedback. I would also like to thank NTNU for offering an extension of the deadline, as the campus was closed for many weeks due to the ongoing Covid-19 outbreak. Lars Lundgaard, André Kapelrud and Dag Linhjell at SINTEF Energy Research have assisted with the laboratory work, which was especially helpful during the weeks with limited lab access. While the scope of the project was limited slightly due to the complicated situation, I'm happy with how it turned out in the end.

I would like to thank to all my fellow students at Department of Materials Science and Engineering for being such good company during long days at the study hall, as well as my parents for support during the final weeks of the project.

This work has been funded by the Research Council of Norway through a Strategic Industry Program (294508).

Abstract

In this project the field dependent conductivity of cyclohexane was investigated using differential charge measurements and finite element modelling. Developing accurate models for the conductivity of dielectrics at high fields will increase our understanding of the breakdown phenomena in electrical insulation materials, and may improve the performance and lifetime of power electronic devices. Measurements have been performed with needle electrodes with 2 and 6 µm tip radius, and at both polarities. When high voltage pulses with short rise times are applied to the plane electrode, a current is induced through the cyclohexane, which gradually decreases until a steady current is established after approximately 10 µs. This shows that the current is space charge limited. The measurements with the 2 µm electrode indicate that there might be charge injection from the needle electrode, as the measurements with positive plane electrode are slightly higher than the ones with a negative plane electrode. Numerical modelling shows that conduction in cyclohexane can not be explained with a simple exponentially field dependent conductivity, and a more complex numerical model is therefore required to accurately describe the system.

Sammendrag

I dette prosjektet har den feltavhengige ledningsevnen til sykloheksan blitt undersøkt med differensielle ladningsmåler og finite element modellering. Nøyaktige modeller for ledningsevnen til dielektriske materialer vil øke forståelsen for sammenbruddsfenomener i elektriske isolasjonsmaterialer, og kan øke ytelsen og levetiden til kraftelektronikk-komponenter. Målinger har blitt gjennomført med nål-elektroder med 2 og 6 µm tuppradius, og ved begge polariteter. Når høyspenningspulser med kort stigetid anvendes på plan-elektroden blir en strøm indusert gjennom sykloheksanen, som gradvis synker inntil en jevn strøm er etablert etter ca. 10 µs. Dette viser at strømmen er romladningsbegrenset. Målingene med 2 µm elektroden indikerer at det kan forekomme ladningsinjeksjon fra nålelektroden, ettersom målingene med positiv plan-elektrode er noe høyere enn de med negativ plan-elektrode. Numerisk modellering viser at elektrisk ledning i sykloheksan ikke kan beskrives med en enkel eksponentielt feltavhengig ledningsevne, og en mer kompleks numerisk modell trengs derfor for å presist beskrive systemet.

Nomenclature

h	Planck constant
k_B	Boltzmann constant
m_e	Electron mass
e	Electron charge
$\mathbf{E}$	Electric field
E	Electric field intensity
ϵ_0	Vacuum permittivity
ϵ_r	Relative permittivity
$\hbar$	Reduced Planck constant
IP_0	Ionization potential at zero field
J	Electric current density
$\mathbf{J}$	Electric current density vector
μ	Charge carrier mobility
n	Charge carrier density
N_d	Number density of dopants
N_{eff}	Effective density of states in the conduction band
Φ	Electrode work function
R	Reflection rate of electrons at electrode surface
σ	Electrical conductivity
T	Temperature
V	Electric potential

Contents

1 Introduction **1**
- 1.1 Background . . . 1
- 1.2 Aim and scope of the work . . . 2

2 Theory **3**
- 2.1 Field dependent conductivity of dielectrics . . . 3
  - 2.1.1 Bulk conduction mechanisms . . . 4
  - 2.1.2 Electrode injection mechanisms . . . 5
  - 2.1.3 Field dependent conductivity of cyclohexane . . . 6
- 2.2 Electroquasistatics . . . 6
- 2.3 Space charge limited fields . . . 7
- 2.4 Pre-breakdown phenomena in dielectric liquids . . . 8
  - 2.4.1 Inception of streamers in cyclohexane . . . 9
- 2.5 Differential charge measurements . . . 10
- 2.6 The finite element method . . . 10

3 Experimental **13**
- 3.1 Experimental setup . . . 13
  - 3.1.1 Test cell . . . 14
  - 3.1.2 Cyclohexane . . . 14
  - 3.1.3 Electrode preparation . . . 14
  - 3.1.4 Differential charge measurements . . . 15
  - 3.1.5 High voltage pulse source . . . 15
  - 3.1.6 Voltage measurements . . . 16
  - 3.1.7 Photomultiplier . . . 16
  - 3.1.8 Computer control and data acquisition . . . 16
- 3.2 Finite element modelling . . . 18
  - 3.2.1 Geometry and meshing . . . 18
  - 3.2.2 Physics and boundary conditions . . . 18
  - 3.2.3 Studies and discretization of time steps . . . 19
  - 3.2.4 Fitting to experimental results . . . 19

4 Results **21**
4.1 Needle electrodes . . . 21
4.1.1 2 µm needle electrode . . . 21
4.1.2 6 µm needle electrode . . . 22
4.1.3 Comparison of needle electrodes . . . 23
4.2 Voltage measurements . . . 24
4.3 Current measurements in cyclohexane . . . 25
4.3.1 Numerical calibration of results . . . 25
4.3.2 Measurements with 2 µm needle electrode . . . 27
4.3.3 Measurements with 6 µm needle electrode . . . 30
4.4 Fitting of numerical model to experimental results . . . 33
4.4.1 Fitting the mean current during the first 10 µs . . . 33
4.4.2 Fitting the mean current from 10 to 40 µs . . . 35
4.4.3 The effect of the rise time on numerical results . . . 38

5 Discussion **39**
5.1 Accuracy and reliability of charge measurements . . . 39
5.1.1 Noise . . . 39
5.1.2 Calibration of charge measurements . . . 40
5.1.3 Discharges and other phenomena at very high voltage . . . 41
5.1.4 Consistency of the measurements . . . 42
5.2 Characteristics of the charge measurements . . . 45
5.2.1 Influence of electrode polarity . . . 45
5.2.2 Influence of electrode tip radius . . . 47
5.2.3 Comparison to previous results . . . 48
5.3 Accuracy of numerical model . . . 48
5.3.1 Parameters for numerical modelling . . . 48
5.3.2 Strengths and weaknesses of the numerical model . . . 49

6 Conclusions **51**

Appendix A MATLAB code for investigating shape of needle electrodes **57**

Appendix B MATLAB code for parameter study **59**

Appendix C Measurements with 2 µm needle and positive plane electrode **63**

Appendix D Measurements with 2 µm needle and negative plane electrode **66**

Appendix E Measurements with 6 µm needle and positive plane electrode **69**

Appendix F Measurements with 6 µm needle and negative plane electrode **72**

Chapter 1

Introduction

1.1 Background

Power electronics are central to the power grids that transfer electricity between the suppliers and consumers of electricity, because they facilitate transfer of power between different electrical systems [1, 2]. The power grids are currently undergoing rapid changes. The increased use of renewable energy sources, like wind and solar power, result in a more dispersed and irregular power production [1, 3, 4]. As these energy sources depend on external conditions outside of our control, it is difficult to adapt the power production to the power consumption. Because of this, a more flexible power grid is required to incorporate these energy sources properly. The power plants also need to be located where the conditions are suitable for power production, unlike fuel based power production, which can be built at any suitable strategic location. Consequentially, a large, complex grid with many dispersed generation units is developed, which requires more advanced power electronic technology to operate efficiently.

This creates an increased demand for power electronic devices with high power rating and switching frequency. New devices based on wide-bandgap semiconductors such as SiC and GaN promise better efficiency and higher temperature tolerance than conventional Si based devices [2, 5]. However, the high voltages and steep rise times cause higher strains on the electric insulation, and may lead to partial discharges that limit device performance [6]. In spite of this, the factory acceptance stress tests currently used are still based largely based on slow, conventional sinusoidal voltages, which have been found incomparable to the real working conditions of the devices [5]. Further research should therefore be done to investigate the performance of dielectric materials under the relevant working conditions.

Accurate estimates of the electric field within the dielectric are important to predict the lifetime of the components, as the initiation of the breakdown phenomena are highly field dependent [5–8]. However, at high fields the charge distribution within the dielectric may change, which complicates the estimations of the local electric field [9]. This charge accumulation is governed by the field dependent conductivity of the dielectric. Developing accurate

models for the field dependent conductivity of dielectrics will therefore aid in predicting the lifetime of power electronic devices.

1.2 Aim and scope of the work

This project aims to investigate the field dependent conductivity of cyclohexane using differential charge measurements and finite element modelling. Cyclohexane shares many of the properties of the electrical insulation materials used in power electronic devices, and understanding the behavior of cyclohexane at high electric fields will aid in predicting how other dielectrics behave under similar conditions. The availability of literature on the behavior of cyclohexane at high electric fields also make it a prime candidate for testing the experimental and numerical methods used in this work.

The experiments will utilize a test cell with a needle-plane geometry and an additional probe electrode to measure currents through cyclohexane when high voltage pulses are applied to the plane electrode. Measurements will be performed with two different needle electrodes and at both polarities, to investigate the effects of electrode radius and polarity. The results will subsequently be compared to numerical results from finite element modelling in COMSOL Multiphysics to estimate the conductivity of cyclohexane.

Chapter 2

Theory

2.1 Field dependent conductivity of dielectrics

Because dielectrics have a large band gap between the valence and conduction band, their electrical conductivity is negligible under most circumstances. However, it has been found that the electrical conductivity of dielectrics increases with increasing electric field [7, 9–11]. This section will present existing theory for electrical conduction in dielectrics, and describe how it relates to the electric field.

The electrical conductivity σ of a material is determined by the charge carrier density n and the charge carrier mobility μ:

$$\sigma = ne\mu \tag{2.1}$$

where e is the electron charge. The increased electrical conductivity at higher fields indicates that the charge carrier density and/or mobility is increases with electric field. Carrier density may increase by charge injection from the electrodes, or increased delocalization of charge carriers in the bulk material, while the increased mobility is likely a consequence of a lowering of potential barriers between localized sites.

Most models for electrical conduction in dielectrics predict some sort of exponentially field dependent conductivity. Because of this, they may be approximated by a conductivity of the form:

$$\sigma(E) = \sigma_0 \cdot \exp\left(k \cdot \sqrt[n]{E}\right) \tag{2.2}$$

where E is the electric field intensity, σ_0 is the conductivity at zero field, and k and n are constants. In the following sections some of the mechanisms for conduction in dielectrics will be presented, and their field dependence will be highlighted.

2.1.1 Bulk conduction mechanisms

Hopping conduction

Hopping is a sudden displacement of a charge carrier from one localized site in the dielectric to another localized site [7, 12, 13]. When an external electric field is applied, the potential barrier that localizes the charge carriers is lowered, resulting in an increased carrier mobility [12]. Because the charge carrier can overcome the potential barrier through either excitation over the barrier, tunneling through the barrier or thermally assisted tunneling, there are many different models for hopping conduction in dielectrics. A commonly used model for hopping conduction in dielectrics is the sinh law of conduction [12]:

$$\sigma(E) = \frac{2\nu aen}{E} \exp\left(-\frac{W}{k_B T}\right) \cdot \sinh\left(\frac{eEa}{2k_B T}\right) \tag{2.3}$$

where ν is the phonon frequency, a is the inter-trap distance, W is the trap depth, k_B is the Boltzmann constant and T is the temperature. At sufficiently high fields high fields, this equation may be reduced to Equation 2.3 with $n = 1$. This model neglects tunneling, and only considers excitation over barrier. While the model was originally derived for ionic motion in crystals, it has also been used for electron- and hole-migration in amorphous dielectrics [12, 14].

Poole-Frenkel conduction

In the presence of an electric field, the potential barriers that localize charge carriers within the dielectric will be lowered, and may increase the charge carrier concentration if donors or acceptors are present [7]. As the band gap in dielectrics is very wide, the energy required to donate electrons to the conduction band or accept electrons from the valence band is larger than the available energy at room temperature, unlike what is the case for doped semiconductors [7]. However, when an electric field is applied, the potential barrier localizing the electron is reduced. By considering the Coulomb interactions between the ionized dopant and the escaping charge carrier, there has been estimated a conductivity of [7]:

$$\sigma(E) = \sqrt{N_{eff} N_d} \cdot e\mu \cdot \exp\left(-\frac{IP_0}{2k_B T}\right) \cdot \exp\left(\frac{\sqrt{e^3 E}}{k_B T \sqrt{4\pi\epsilon_r \epsilon_0}}\right) \tag{2.4}$$

where N_{eff} is the effective density of states in the conduction band of the dielectric, N_d is the number density of dopants, IP_0 is the ionization potential of the dopants at zero field, ϵ_r is the relative permittivity of the dielectric and ϵ_0 is the vacuum permittivity. The field dependence of Poole-Frenkel conduction is described by Equation 2.2 with n=2.

2.1.2 Electrode injection mechanisms

Injection of charge carriers from the electrodes is dependent on the electrodes used, as well as the polarity of the electrode, and is not an intrinsic property of the material. However, it is important to consider how susceptible the material is to charge injection both when investigating it in a laboratory setting, and when it is used in practical applications.

Schottky injection

Schottky injection is injection of majority charge carriers from the electrodes, which increases the charge carrier concentration in the material. The resulting current may be estimated by considering Coulomb interactions between an escaping electron and the electrode, the electrode will be left positively charged when the electron escapes. The attractive Coulomb force between the electron and the electrode will act as an barrier against charge injection, but when an electric field is applied, this barrier is lowered. The resulting current density is shown to be [7]:

$$J = \frac{4\pi e m_e k_B^2 (1-R) T^2}{h^3} \cdot \exp\left(-\frac{\Phi_{eff}}{k_B T}\right) \tag{2.5}$$

where m_e is the electron mass, R is the reflection rate of electrons at the electrode surface and h is the Planck constant. Φ_{eff} is the effective potential barrier [7]:

$$\Phi_{eff} = \Phi - \frac{e}{2}\sqrt{\frac{eE}{\pi \epsilon_r \epsilon_0}} \tag{2.6}$$

where Φ is the electrode work function, ϵ_r is the relative permittivity of the dielectric and ϵ_0 is the vacuum permittivity.

Fowler-Nordheim injection

Charge may also be injected into the dielectric by quantum-mechanical tunneling when the electric field near the electrode is very high ($\approx 10^9$ V/m) [7]. Because electrons exhibit wave-like properties, they may penetrate the potential barrier, despite having inferior energy to the barrier height. If the one-dimensional Schrödinger equation is solved for a triangular barrier, the current density is given by [7]:

$$J = \frac{e^3 E^2}{8\pi h \phi} \cdot \exp\left(-\frac{4}{3}\sqrt{\frac{2m_e}{\hbar^2}}\frac{(\Phi - E_f)^{3/2}}{eE}\right) \tag{2.7}$$

where $\hbar$ is the reduced Planck constant and E_f is the Fermi energy of the electrode. By considering a triangular barrier, Coulomb interactions between the electrode and electron have not been considered. However, these have been found to have a negligible effect on the current density [7].

2.1.3 Field dependent conductivity of cyclohexane

The existing research on the field dependent conductivity of cyclohexane is quite limited, but some attempts at measuring it has been performed. Measurements in a homogeneous field has been fitted to a simple exponentially field dependent conductivity of [14]:

$$\sigma(E) = 1.5 \cdot 10^{-12}\,\mathrm{S/m} \cdot \exp\left(1.12 \cdot 10^{-3}\,\mathrm{C^{0.5}/N^{0.5}} \cdot \sqrt{E}\right) \tag{2.8}$$

which matches the field dependence predicted by Poole-Frenkel conduction and Schottky injection. However, the sample size in this analysis was quite small, and the model underestimated the pre-inception current at voltages above 9 kV.

The author has previously performed preliminary measurements with a 2 µm needle electrode at negative polarity. Subsequent finite element modelling estimated a conductivity of [15]:

$$\sigma(E) = 1.5 \cdot 10^{-12}\,\mathrm{S/m} \cdot \exp\left(1.5 \cdot 10^{-7}\,\mathrm{C/N} \cdot E\right) \tag{2.9}$$

which indicates that hopping conduction is the dominating conduction mechanism. There were, however, multiple complications during the experiments. The needle electrode was bent sometime during the experiments, which complicates the comparison of experimental and numerical results. In addition, measurements were only performed with one polarity, and the resulting fit between numerical and experimental results was imperfect. The results also differ from what has previously been reported. Because of this, there is still no established model for the field dependent conductivity of cyclohexane.

2.2 Electroquasistatics

Electroquasistatics analysis is a generalization of electrostatics, which describes the electric field in a perfect dielectric material, and steady currents, which describes highly conductive materials [16]. This approach assumes that the changes in magnetic potential due to the movement of charges in the system are negligible, and allows us to work with a time-varying scalar electric potential. In this case, the electric field is given by the gradient of the electric potential [17]:

$$\mathbf{E} = -\nabla V \tag{2.10}$$

where V is the electric potential and $\mathbf{E}$ is the electric field.

When voltage is applied to one of the electrodes in the system, the resulting current will be sum of the *displacement current* and the *conduction current*. The displacement current is related to the permittivity of the media and change in electric field, while the conduction current is the flow of electrical charges between the electrodes. The total current density is [16]:

$$\mathbf{J} = \sigma\mathbf{E} + \epsilon_r\epsilon_0\frac{\partial\mathbf{E}}{\partial t} \tag{2.11}$$

where $\mathbf{J}$ is the electric current density vector. The first term corresponds to the conduction current and the second term is the displacement current.

Current conservation relates the electric current density to the charge density [16]:

$$\boldsymbol{\nabla}\cdot\mathbf{J} = -\frac{\partial\rho}{\partial t} \tag{2.12}$$

In systems where there is no net space charge present (i.e. ρ=0), Equation 2.12 satisfies Laplace's equation:

$$\nabla^2 V = 0 \tag{2.13}$$

and the field in this case is accordingly referred to as a *Laplacian field*.

2.3 Space charge limited fields

In materials with field dependent electrical conductivity, high field regions will result in local variations in conductivity. This may lead to charge separation and buildup, which limits the total field in this region. The resulting field is referred to as a *space charge limited field*. During use, a dielectric material may be exposed to high field regions due to high operating voltages and defects such sharp protrusions from the conductor or metallic contamination [18]. The electric field in these regions may be space charge limited when sufficiently high voltage is applied, and will not increase significantly when the voltage is increased further [9]. However, the size of the high field region will continue to increase at higher voltages.

For the space charge limited field to establish in the material during AC-currents or voltage pulses with short rise times, the dielectric time constant must be comparable to the inverse of the applied frequency [9]:

$$\frac{1}{\omega} \approx \tau \tag{2.14}$$

where ω is the voltage frequency and τ is the dielectric time constant. The dielectric time constant is given by:

$$\tau = \frac{\epsilon_r \epsilon_0}{\sigma_{SCLF}} \tag{2.15}$$

where σ_{SCLF} is the conductivity in the space charge limited field.

For high frequency AC voltages or voltage pulses with short rise times, it may not always be clear whether the system can redistribute charge quickly enough to limit the field. Because of this, accurate models for the conductivity are necessary to estimate the field in dielectrics. If the permittivity of the material is independent of the electric field, and the conductivity of the material is of the form of Equation 2.2, the space charge limited may be estimated as [19]:

$$E_{SCLF} \approx \left(\frac{1}{k} \cdot \ln \frac{\epsilon_r \epsilon_0 \omega}{\sigma_0} \right)^n \tag{2.16}$$

where E_{SCLF} is the space charge limited field. This is a quite crude approximation, as it is based on the approximation presented in Equation 2.14. However, it does show general trends for how the space charge limited field varies with the conductivity of the material. For a material with highly field dependent conductivity, i.e. high k- and low n-parameters, the space charge limited field will be quite low, as the difference in conductivity in the high- and low-field regions will be very different.

2.4 Pre-breakdown phenomena in dielectric liquids

At sufficiently high fields, the insulating properties of dielectrics break down. In dielectric liquids, the breakdown is usually preceded by a *streamer* propagating through the material. Streamer is a common term for all pre-breakdown in liquids which involve vaporization and can be observed through schlieren/shadow graphics [21]. They typically form tree-like structures, as shown in Figure 2.1, which are similar to the electric trees observed in solid insulation materials. However, because of the self-healing properties of liquids, the structures are not permanent. A streamer is classified by the electrode from which it propagates, i.e. a streamer propagating from the negative electrode is called a negative streamer, and the inception voltage for streamers is typically lower for negative streamers than positive streamers [21].

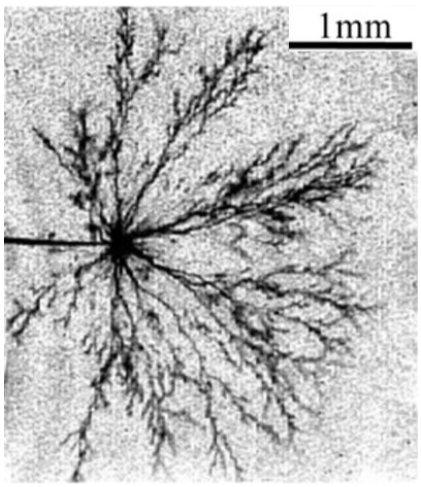

Figure 2.1: Image of positive streamer in mineral oil. Figure adapted from [20].

The initiation of streamers is highly field dependent [5–8], and the lifetime of a power electronic component will affected by many different factors. In addition to the operating voltage level, polarity and frequency, sharp pieces of conductive material, either in the form of metallic contamination or surface defects on the electrode, will result in significantly higher fields and breakdown probability [19]. As discussed in Section 2.3, charge accumulation within the dielectric may also change the field distribution in the material. Accurate models for the conductivity of the dielectric, which controls the space charge limited field, is therefore necessary to achieve good estimates for the lifetime of power electronic components.

The mechanism for streamer inception differs between positive and negative streamers. Negative streamers are initiated by a discharge in liquid phase, which causes formation of bubbles and subsequent discharges occur in these bubbles [8, 21, 22]. While the mechanisms for initiation of positive streamers are yet to be determined [21], several theories have been proposed. Since the inception of positive streamers has been found to vary with the hydrostatic pressure [8], it is assumed that the streamer is initiated by discharges in gas- or low density-regions within the dielectric. These regions may form due to local joule heating [8] or electromechanical forces as a consequence of the applied field [23].

2.4.1 Inception of streamers in cyclohexane

The initiation of streamers in cyclohexane in a needle-plane geometry has been previously been researched, and the influence of various experimental parameters have been investigated . The inception voltage has been found to be nearly independent of the rise time of the applied voltage [8], but increases with increasing plane-needle distance [24]. The inception voltage also increases with increasing tip radius of the needle electrode, as shown in Figure 2.2. As these experiments were performed with a positive needle electrode, a slightly lower inception voltages should be expected for measurements performed with a negative needle electrode.

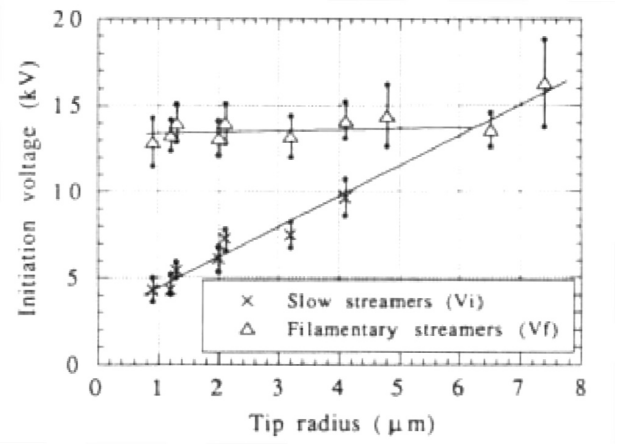

Figure 2.2: Inception voltage for positive streamers in cyclohexane with a needle-plane distance of 2.5 mm and rise times lower than 15 ns. Figure adapted from [24].

2.5 Differential charge measurements

Specialized measurement techniques are required to measure conduction currents in dielectrics. Due to the low conductivity of the material and high applied voltages, the resulting displacement current is much larger than the conduction current. Because of this, it is difficult to design a measurement system that has sufficient detection range to measure the displacement current, while also having sufficient sensitivity to measure the conduction current [8, 24].

Differential measurement techniques are commonly used to isolate the contributions of the conduction current from the total current. These techniques typically utilize a needle plane geometry with an additional blunt probe electrode [8, 21, 24]. The electric field near the needle electrode is magnified due the sharp curvature, which correspondingly increases the conductivity of the dielectric, as described in Section 2.1. For that reason, it is assumed that only the charge injected at the needle electrode will have contributions from the conduction current. The setup is calibrated by adjusting the height of the needle and probe electrodes until the needle-plane and probe-plane capacitances are equal. The induced displacement current on the two electrodes will then be equal, assuming the permittivity of the material is independent of the electric field, and the conduction current induced at the needle electrode can be estimated as the differential current between the two electrodes. This technique has achieved a maximum sensitivity of around 10 µA [24].

The sensitivity of the measurements has been further increased by measuring the charge induced on two measurement capacitors, instead of directly measuring the current. The injected charge induces a voltage over the measurement capacitors of:

$$\Delta V = \frac{Q}{C_m} \tag{2.17}$$

where Q is the induced charge and C_m is the capacitance of the measurement capacitors. By using differential charge measurements, it is possible to detect charges below 0.1 pC, which allows for measurements of very small currents [8].

2.6 The finite element method

The finite element method is commonly used to analyze real systems and investigate the effect of different parameters on the overall behavior of the system [19, 25]. The general goal of the finite element method is to solve a set of partial differential equations, which describe the physics of the system, for a given geometry and boundary conditions. These differential equations are often impossible to solve analytically [16, 19], necessitating the use of numerical approximations.

In the finite element method, the geometry is divided into a finite number of sub-domains in a process called *discretization* or *meshing*. A set of linear equations is created for each

element from the partial differential equations to be solved, creating one large equation set. This equation set are then solved using numerical methods such as Newton's method or Runge-Kutta methods. If a small mesh size is created, the domain structure will approximate the continuous domain of the real system, and good numerical approximations can be achieved. However, decreasing mesh size will also increase the size of the equation set, and consequentially the computational time increases. To achieve an optimal combination of accuracy and efficiency, it is often useful to create a non-uniform mesh. This way a small mesh size can be used in regions where the gradient of the different parameters is large, to achieve high accuracy, and a larger mesh size can be used in more homogeneous regions of the system, to decrease the computational time. In the case of time-dependent studies, the same principle may be utilized for the discretization of the time range of the study, to create a non-uniform time-discretization.

The models developed have many different use cases. One use case is to estimate the value of an unknown variable within the system that is difficult to measure directly. This can be done by comparing the numerical results to experimental results, and tweak the values of the unknown parameters until the experimental and numerical results match. Once the model has been found to accurately predict the behavior of a real system, it may also be used to improve the design of components and devices. As the numerical modelling is both faster and cheaper than developing working prototypes, it is possible to test a multitude of different design parameters, to find the parameters that optimize the device performance. However, it is advisable to verify the results experimentally, as no model will ever be completely accurate.

Chapter 3

Experimental

3.1 Experimental setup

The experimental setup used in this work is a modified version of a setup developed in an earlier project [15]. A sketch of the experimental setup is presented in Figure 3.1. 1:1 isolation transformers and optical separators were used to avoid ground loops, and ferrite cores were mounted on the cables to improve high-frequency resistance. This was done to minimize the noise from ambient electromagnetic radiation. In the following sections the individual parts of the setup will be described in detail.

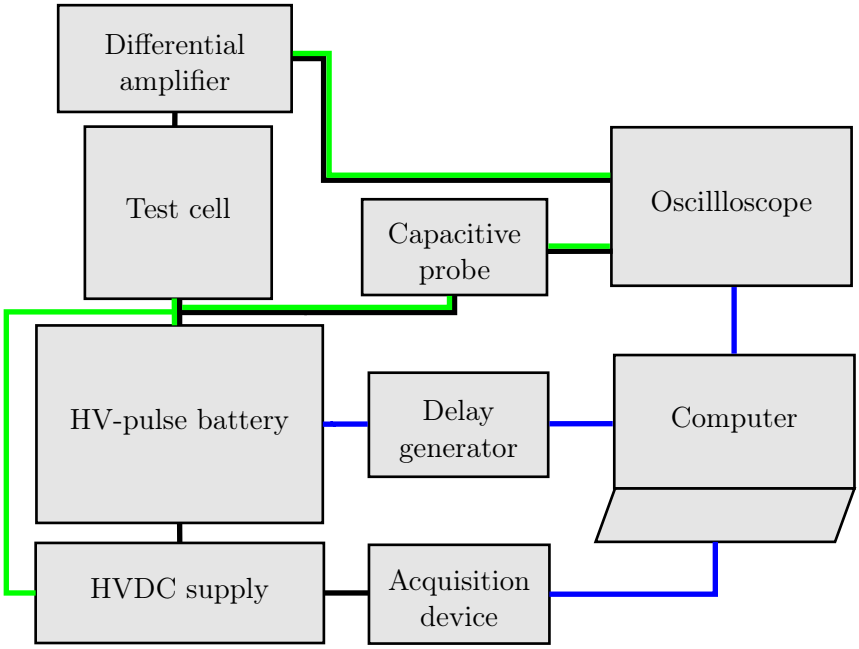

Figure 3.1: Sketch of experimental setup. Black connectors represent non-grounded electrical contacts, green connectors represent grounded contacts and blue connectors represent optical connections.

3.1.1 Test cell

A sketch of the test cell used for the measurements is presented in Figure 3.2. The test liquid is contained within a 3 dl glass cylinder, with a steel plane electrode underneath and a steel lid with two feedthroughs above. A probe and a needle electrode are mounted on the feedthroughs. After calibration, the 2 µm and 6 µm needle electrodes were placed 7.5 and 7.0 mm above the plane electrode, respectively.

The volume surrounding the glass cylinder has previously contained a circulation liquid for temperature control [21], but for this work it was simply filled with air, as measurements were performed at room temperature. The outer casing of the cell is made of stainless steel, but contain two double pane evacuated windows for external observation and photomultiplier measurements. High voltage pulses are applied to the plane electrode through a feed through at the bottom of the cell.

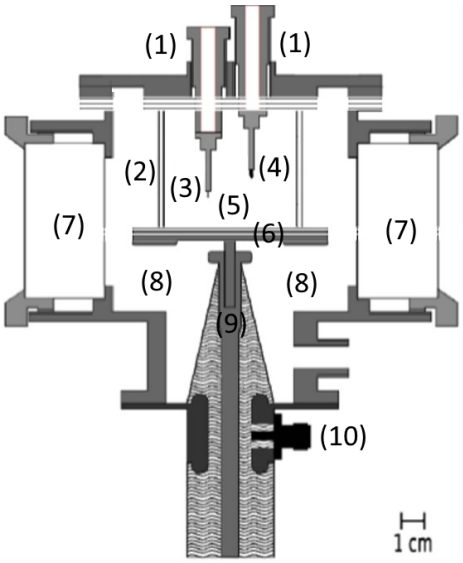

Figure 3.2: Sketch of test cell with needle-plane geometry. (1) Electrode feedthroughs, (2) glass cylinder, (3) needle electrode, (4) probe electrode, (5) sample volume, (6) plane electrode, (7) evacuated windows, (8) circulation volume, (9) high voltage feedthrough and (10) capacitive high voltage probe. Figure adapted from [21].

3.1.2 Cyclohexane

Measurements were performed on EMSURE®110-82-7 cyclohexane with at least 99.5 % purity [26]. As cyclohexane is very volatile and should not be inhaled , the test cell was filled under a fume hood and sealed before it was returned to the test setup.

3.1.3 Electrode preparation

The needle and probe electrodes were prepared by electrochemical etching. The etching was performed in 2 M NaOH solution at 10 V in cycles of approximately 5 seconds. In between each cycle the electrode was investigated with a Keyence VHX-600 digital light microscope at 1000x magnification. This process was repeated until the desired geometry was achieved.

For the needle electrodes, wolfram wires with a diameter of 100 µm were inserted into a 0.7 mm stainless steel canulla and etched to tip curvatures of 2 µm and 6 µm. The probe electrodes were prepared from the steel canullas, which were polished with sandpaper and etched to ensure a smooth surface.

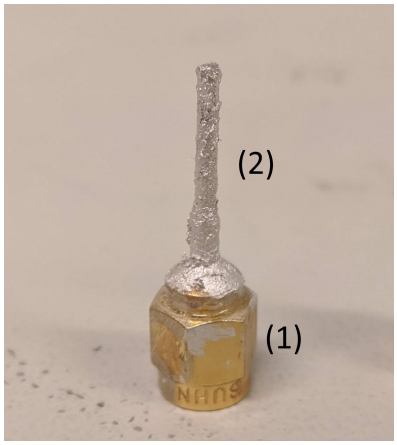

Figure 3.3: Holder for the probe and needle elctrodes. (1): SMA-connector, (2): polytetrafluorethylene tube coated with silver epoxy and transparent epoxy.

One of the electrode holders is shown in Figure 3.3. They consist of an SMA-connector, to connect to the feed throughs, and a polytetrafluorethylene tube where the electrodes are inserted. These tubes were coated with a Epo-Tek H27D silver epoxy for electromagnetic shielding and connecting the two pieces together, and were cured at 150 °C for one hour. An additional layer of Epo-Tek 303-3M transparent epoxy was added and was cured at 65 °C for 3 hours to improve the structural integrity.

The needle electrodes were investigated in a Zeiss Supra 55 Scanning Electron Microscope before and after they were used for measurements. Imaging was performed with a secondary electron detector, 10 kV acceleration voltage and 10 mm working distance. Each needle was observed from three different angles, to investigate if the needle is symmetrical. To compare the shape of the tip of the needle electrode before and after experiments, a MATLAB [27] script was created to extract the shape of the needle electrode. This script is available in Appendix A.

3.1.4 Differential charge measurements

The needle and probe electrodes were connected to two measurement capacitors of 472 pF and a LeCroy DA1855A differential amplifier. A cicruit diagram of the setup is presented in Figure 3.4. The differential amplifier was set to 1X gain, 1X attenuation and 100 MΩ input resistance. To calibrate the setup, pulses of 1 kV were applied to the plane electrode, and the height of the electrodes were adjusted to minimize the initial currents measured, which indicates that the needle-plane and probe-plane capacitances are equal. However, as the measurements are very sensitive to small displacements of the electrodes, some additional calibration was performed numerically during post-processing of the results.

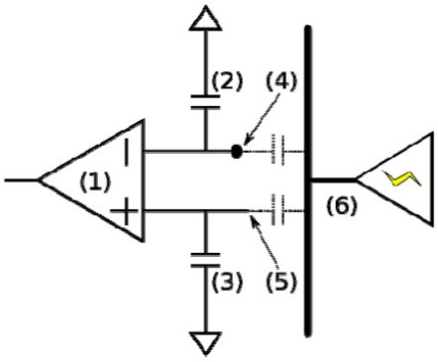

Figure 3.4: Schematic for differential charge measurements. (1) Differential amplifier, (2,3) Measurement capacitors, (4) Probe electrode, (5) Needle electrode, (6) Plane electrode. Figure adapted from [21].

3.1.5 High voltage pulse source

The high voltage pulse battery consisted of two Ceramite 3300 pF capacitors and a fast high voltage MOSFET switch mounted in a grounded closet, and was powered by a Glassmann EH series 40 kV HVDC-supply. A circuit diagram for the high voltage pulse source is presented in Figure 3.5. The various resistors in the pulse battery serve to limit the current below 2.5 mA, which is the limit for the HVDC-supply, and to allow for automatic discharging of remaining charges at the capacitors without short-cutting the circuit.

3.1.6 Voltage measurements

To measure the output of the pulse battery, a capacitive high voltage probe was mounted on the feed through between the pulse battery and the test cell. This is shown in Figure 3.2 (10). The probe was connected to the oscilloscope via a Sigmond BS5 integrator, as Sigmond integrators have been found to improve the measurements of high voltage pulses [28]. This setup has previously been calibrated, and has been found to achieve reliable voltage measurements with a scale factor of 672.84 V/mV [15].

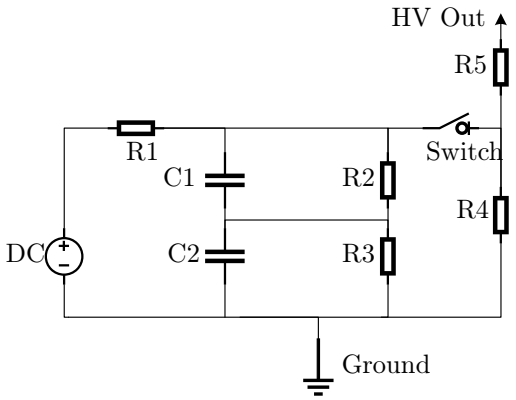

Figure 3.5: High voltage pulse battery. DC = Glassman EH series 40 kV HVDC supply, R1=70 MΩ, R2=R3=500500 MΩ, C1=C2=9900 pF, R4=1 MΩ, R5=1 kΩ. Figure adapted from [15].

3.1.7 Photomultiplier

A Hamamatsu R943-02 GaAs photomoultiplier was originally mounted to monitor light flashes from the experiment. However, recording signals from the photomuliplier, in addition to the voltage probe and differential amplifier, reduced the available resolution for each signal, due to limitations of the oscilloscope. Because the voltages applied were lower than the estimated inception voltages for cyclohexane, the photomultiplier was not used in the experiments. Even if discharges were to occur, it should not be a significant problem, as they could be observed in the charge measurements as well.

3.1.8 Computer control and data acquisition

The setup was controlled by a computer running LABView, allowing for automated measurement sequences. To control the voltage of the applied pulses, the computer was connected to the HVDC source via a NI USB-6008 data acquisition device. This device supplies a 0-5 V signal to the HVDC source, which results in a 0-20 kV output voltage from the voltage source. The HVDC source is capable of voltages up to 40 kV, but this was not possible using the NI USB-6008, as that requires an input signal of 10 V. However, voltages above 20 kV were not necessary for this work.

The switch in the high voltage pulse battery was controlled by an external optical signal. This signal was created by a Stanford DG645 delay generator and converted to an optical signal by an designed for conventional 9-volt battery, but to ensure sufficient battery life for longer measurement sequences, it was connected to a rechargeable car battery.

High voltage pulses of 1-5 kV were applied for the 2 µm electrode, and 2-10 kV for the 6 µm electrode. 10 measurements were performed for each voltage level with intervals of 40 minutes. To investigate whether the system was altered in any way during the measurements, the measurements at each voltage was split into two series of 5 shots. First a series where the voltage was incrementally increased from the minimum to the maximum voltage was

performed, followed by a series at decreasing voltage, starting from the maximum voltage. A test measurement was also performed at 1 kV before each new voltage level, to determine whether any notable changes has occurred to the system during the measurements. The complete measurement sequence is presented in Figure 3.6.

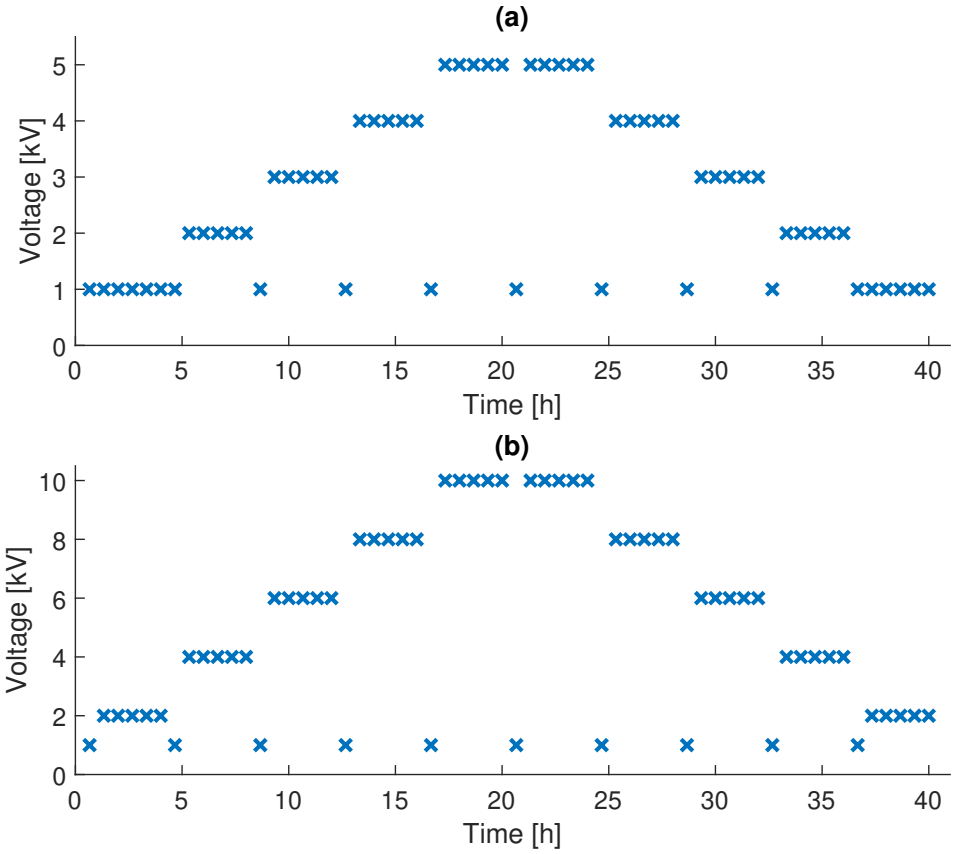

Figure 3.6: Measurement sequences used for the 2 µm (a) and 6 µm (b) needle electrode. Each marker corresponds to a high voltage pulse.

A Tektronix TDS540 oscilloscope was used to record the signal from the high voltage probe, the differential amplifier and the photomultiplier. The recorded wave-forms were read by a LABView program after each shot, and stored as csv-files for post-processing.

3.2 Finite element modelling

3.2.1 Geometry and meshing

Finite element modelling of the system was performed in COMSOL Multiphysics 5.4 [29] to determine the field dependent conductivity of the sample liquid. To replicate the geometry of the needle electrode, Microsoft Excel was used to fit a 2nd order polynomial to the surface profile extracted from the SEM photos of the needle. A 2-dimensional axisymmetric geometry was then developed with the plane electrode at the bottom, the needle electrode and the rest of the volume filled with the sample liquid. The section of the geometry surrounding the 2 µm needle electrode is presented in Figure 3.7.

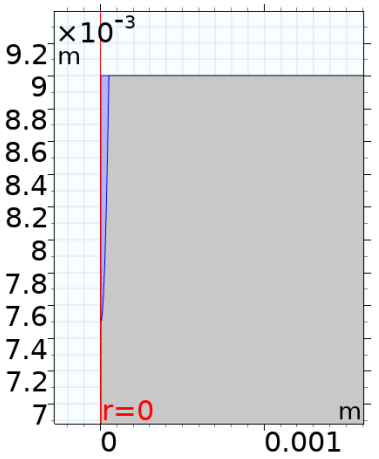

Figure 3.7: Sketch of the geometry near the 2 µm needle electrode in the numerical model. The blue area represents the needle electrode, and the remaining parts of the geometry contains cyclohexane.

COMSOL was used to generate triangular meshes for the geometry, and the resulting mesh size distribution is displayed in Figure 3.8. As the gradient of the electric potential is largest near the needle electrode, a finer mesh was chosen in this region, left of the vertical line in the geometry, while the rest of the geometry uses a larger mesh. A mesh refinement study was performed to find the largest mesh that yielded accurate results. Based on this, the maximum element size near the needle electrode was set to 0.8 mm, while the rest of the mesh had a maximum element size of 14.9 mm.

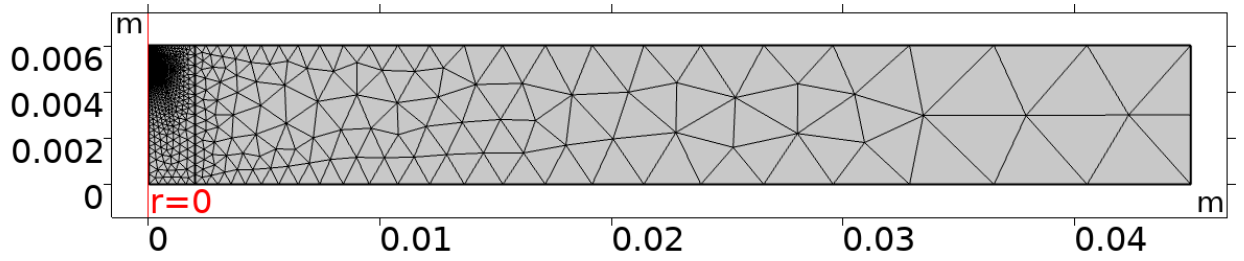

Figure 3.8: Mesh size distribution used for the finite element modelling with the 2 µm needle electrode.

3.2.2 Physics and boundary conditions

The electric field, electric potential, current and charge distribution in the system was calculated with the COMSOL AC/DC module. This module solves Equation 2.10, 2.11 and 2.12 for the given geometry and a set of boundary conditions. The voltage pulse was applied to the bottom boundary of the system, while the needle was set to ground potential, similar to

the experimental conditions. The two remaining boundaries for the system, the right and top borders, were electrically insulated. Please note that the left border of the geometry is a symmetry axis, because of the axisymmetric geometry. The injected charge on the needle electrode was calculated by solving Gauss' law over the surface of the needle:

$$Q = \epsilon_r \epsilon_0 \oiint_S \mathbf{E} \cdot d\mathbf{A} \tag{3.1}$$

where S is a surface surrounding the needle electrode.

3.2.3 Studies and discretization of time steps

The high voltage pulses applied to the plane electrode were replicated as smoothed Heavyside functions with rise times of 50 ns. The smoothed Heavyside function was used instead of a linear ramp to better approximate the behavior of the voltage pulse, as well as avoid numerical errors due to the discontinuous derivatives at the start and end of the linear ramp. The voltage profiles of applied pulses of 1-5 kV, which were used for the modelling with the 2 µmelectrode, are presented in Figure 3.9. After the initial rise, the voltage was kept constant for 40 µs.

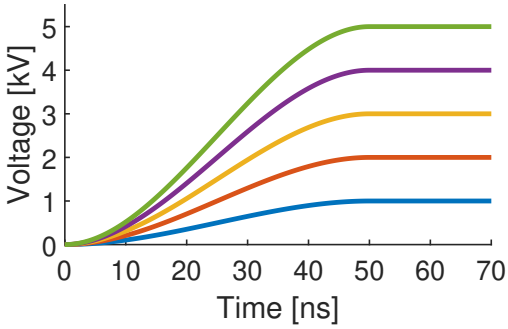

Figure 3.9: Voltage profiles used in numerical simulations for pulses of 1-5 kV.

As the changes in the system are much larger during the rise time of the pulse than during the following voltage plateau, a non-uniform time discretization was chosen. For the first 500 ns the interval between each timestep was 1 ns, while the rest of the modelling was performed with 500 ns time steps.

3.2.4 Fitting to experimental results

All simulations were performed with both a field dependent conductivity of the form of Equation 2.2 and a completely non-conductive material, and the conduction current was found as the difference between the results. This emulates the behavior of the differential charge measurements, were one of the electrodes only experiences the displacement current and the other one has contributions from both the displacement and conduction current.

The COMSOL model was run with different different models for the conductivity of the cyclohexane by varying the parameters n, σ_0 and k. The ranges for the different parameters in the parameter study are presented in Tabel 3.1. A MATLAB [27] script, available in Appendix B, was used to automate the process. This script utilizes COMSOL LiveLink for for MATLAB to change the parameters in the model, run the defined studies and extract the

results. The estimated conduction current was subsequently compared to the experimental results to determine the best conductivity fit for the experimental data.

$n\,[-]$	$\sigma_0\,[\mathrm{S/m}]$	$k\,[(\mathrm{C/N})^{1/n}]$
1	$10^{-13} - 10^{-8}$	$10^{-9} - 10^{-7}$
2	$10^{-13} - 10^{-8}$	$10^{-5} - 10^{-3}$
3	$10^{-13} - 10^{-8}$	$10^{-3} - 10^{-1}$

Table 3.1: Range of parameters used while fitting the numerical model to experimental results.

Chapter 4

Results

4.1 Needle electrodes

4.1.1 2 µm needle electrode

Secondary electron images of the 2 µm needle electrode before and after experiments are presented in Figure 4.1. Before the experiments, the needle is smooth and clean. The surface profile of the needle was fit to a second order polynomial:

$$r_{2\,\mu m}(x) = 610311x^2 + 0.2432x \tag{4.1}$$

where the x-axis is along the longitudinal axis of the needle, $x = 0$ at the tip of the needle and x is measured in meters.

Due to delays during the experiments, this electrode was stored inside the cell for a total of 101 days. During this time period, the cyclohexane had evaporated from the cell. Some high voltage pulses were accidentally applied while the cell was empty, resulting in discharges in air. However, this does not appear to have affected the shape of the needle. Some contamination is present on the surface of the needle after the experiments, including at the tip of the needle itself, but the shape of the needle itself is unchanged.

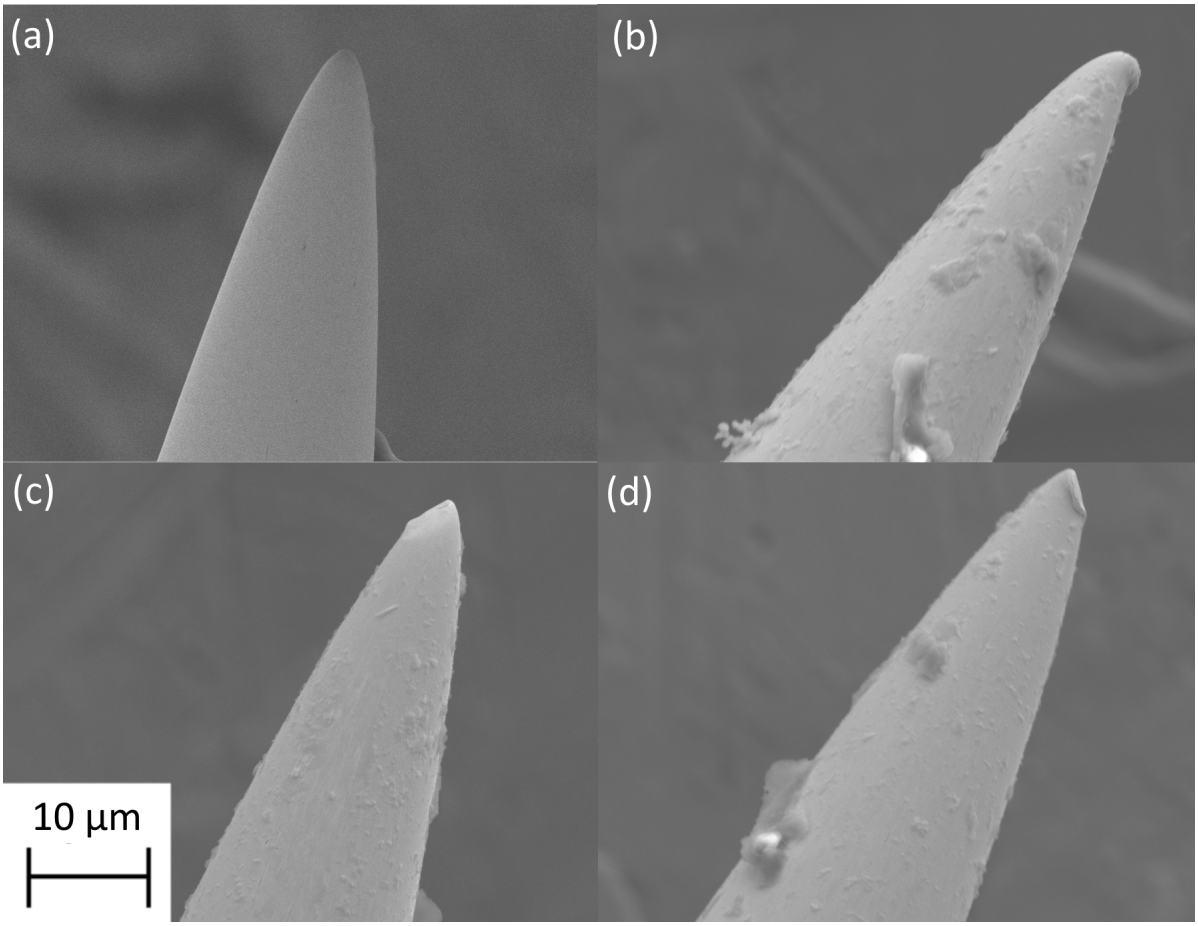

Figure 4.1: Secondary electron images of the 2 µm electrode before experiments (a) and after it was used in measurements (b,c,d).

4.1.2 6 µm needle electrode

Secondary electron images of the 6 µm electrode is presented in Figure 4.2. This electrode was only stored inside the test cell for 24 days. The images of the needle before (a) and after (b) the experiments are almost indistinguishable from each other, and both show a smooth, clean surface. The surface profile of the needle before the experiments was fit to the polynomial:

$$r_{6\,\mu m} = 166878x^2 + 0.01325x \tag{4.2}$$

where the x-axis is along the longitudinal axis of the needle, $x = 0$ at the tip of the needle and x is measured in meters.

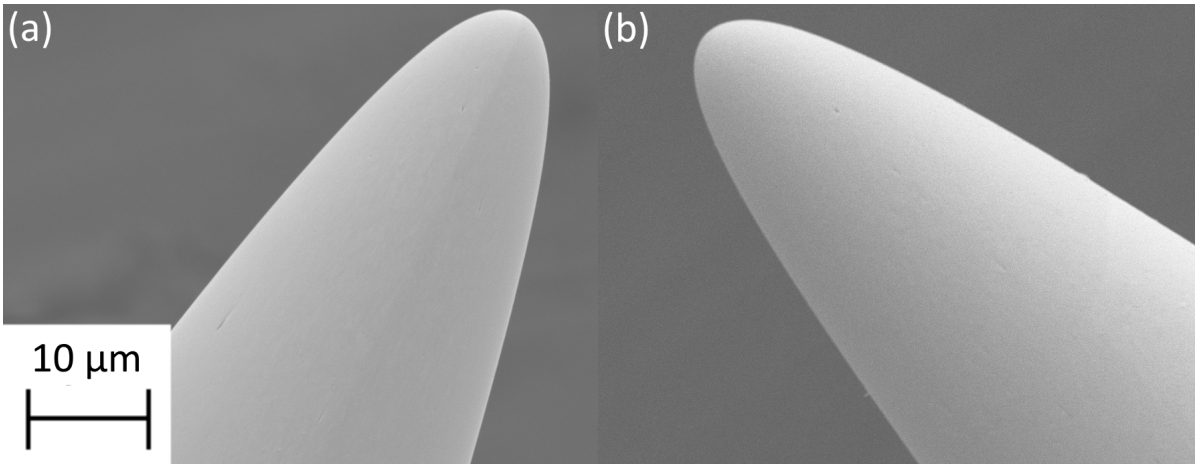

Figure 4.2: Secondary electron images of the 6 µm electrode before experiments (a) and after it was used for measurements (b).

4.1.3 Comparison of needle electrodes

A comparison of the 2nd order polynomials fitted to to each of the needle electrodes is presented in Figure 4.3. These polynomials where used in the numerical model of the system for fitting to experimental results.

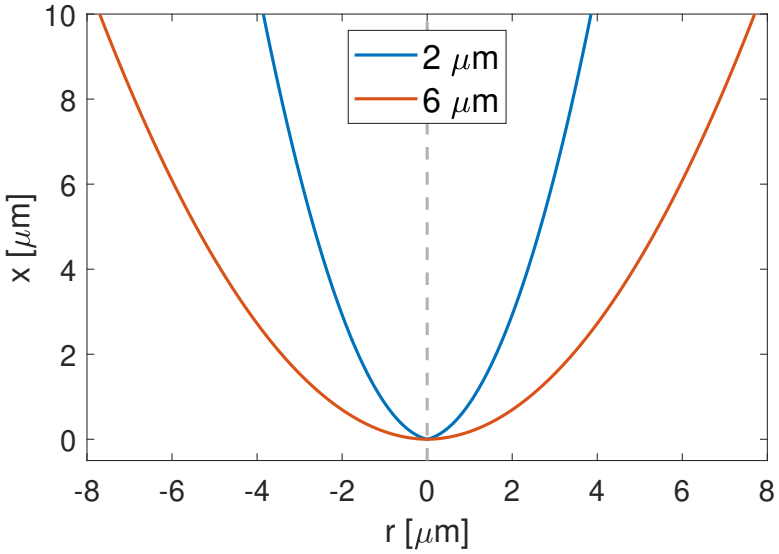

Figure 4.3: Comparison of the two needle electrodes used during measurements.

4.2 Voltage measurements

The voltage profiles of the high voltage pulses applied during the measurements with each of the two needle needles are presented in Figure 4.4 and 4.5. The results are very consistent with low variance, and there is no apparent difference between the two polarities. All the profiles have a slight overshoot at the beginning of the pulse before reaching a stable voltage. At the end of the pulse, after 50 µs, there is a small jump in voltage, before the voltage gradually decreases. The rise time from 0 to the peak voltage increases slightly with increasing voltage, from approximately 40 ns at 1 kV to approximately 60 ns at 10 kV.

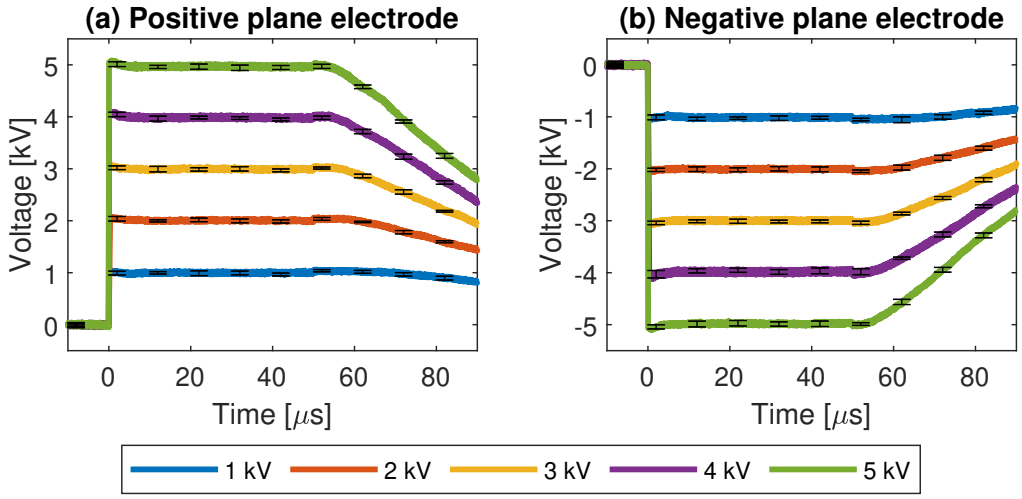

Figure 4.4: Voltage profiles recorded during measurements with the 2 µm electrode. Each curve is the mean value of the 10 pulses applied at each voltage, with the standard deviation plotted as errorbars every 10 µs.

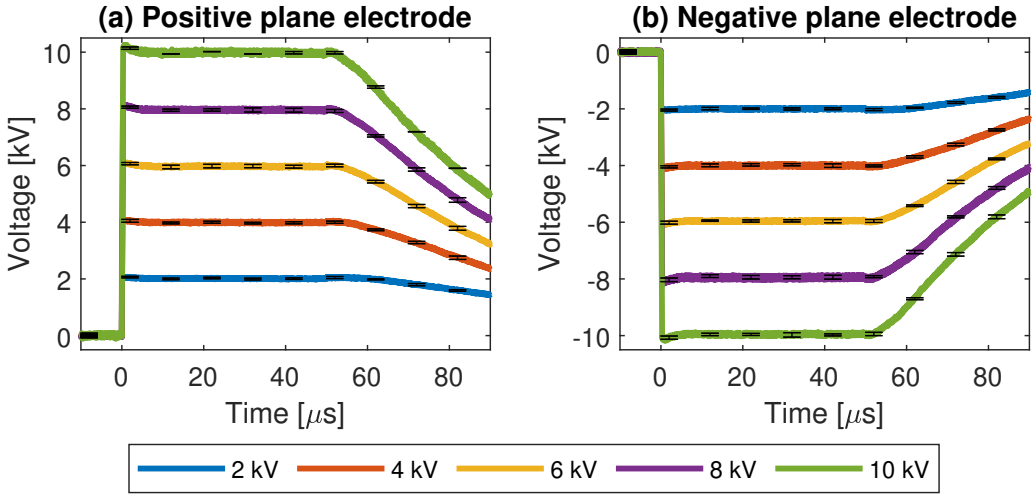

Figure 4.5: Voltage profiles recorded during measurements with the 6 µm electrode. Each curve is the mean value of the 10 pulses applied at each voltage, with the standard deviation plotted as errorbars every 10 µs.

4.3 Current measurements in cyclohexane

4.3.1 Numerical calibration of results

While the differential charge measurements were calibrated before the experiments started, some signs of miscalibration were observed in the results. In this section these problems will be illustrated and the procedures performed during post-processing to fix them will be described.

Figure 4.6a shows the charge measurements during the second shot applied at 10 kV with the 6 µm and negative plane electrode. When the high voltage pulse is applied, the charge quickly drops to ≈ -0.20 pC and rises to $\approx +0.45$ pC, before it stabilizes at ≈ 0.2 pC from about 100 ns. After these rapid changes the first few nanoseconds, the charge increases more gradually. This behavior was observed for most of the measurements, to varying degrees. The initial drop and overshoot was found to increase with increasing voltage, while the charge where it stabilizes varied from shot to shot. During numerical calibration, the charge after these initial oscillations was subtracted manually from the results, leaving only the more gradual currents to contribute to the net charge. This is shown for the previously described measurement in Figure 4.6b.

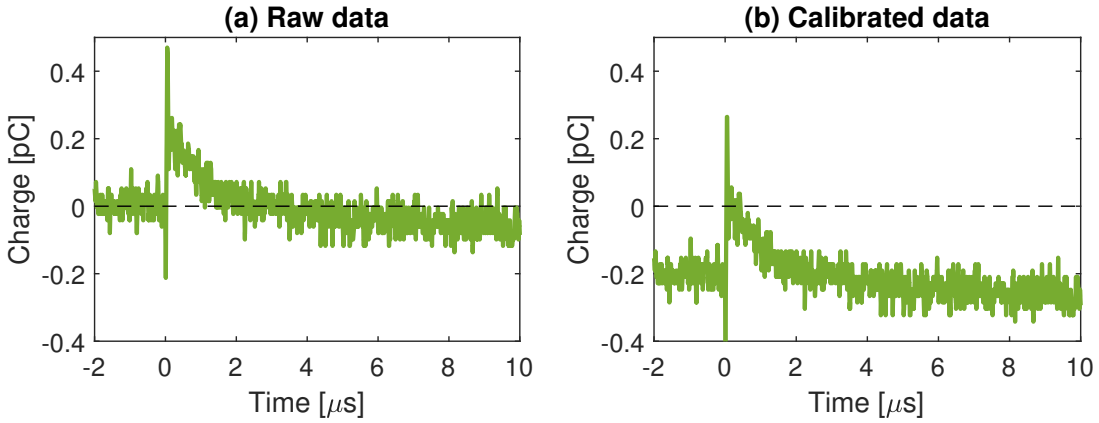

Figure 4.6: Charge measurements during the first shot applied at 10 kV with the 6 µm electrode and a negative plane electrode. The first and second plot shows the results before and after numerical calibration.

This procedure was repeated for each of the 50 shots performed for each measurement series. The charge subtracted during numerical calibration for the measurements with the 2 µm needle electrode is presented in Figure 4.12. Each shot is plotted chronologically. The first 25 shots are 5 shots per voltage while increasing the voltage, while the last 25 shots are 5 shots per voltage while decreasing the voltage. The measurements at the highest voltages are therefore found in the middle of the plot, while the lowest voltages are found to the left and right.

The calibration charge for the measurements with positive plane electrode is very small for

all the shots, ranging from -0.05 pC to +0.02 pC. There appears to be a slightly larger negative shift for the measurements at 10 kV and the last 5 shots at 8 kV than for the other measurements. However, the variance is quite large, which makes it difficult to observe any clear trends. For the measurements with the negative plane electrode, on the other hand, the calibration charge increases quite systematically with increasing voltage during the first 25 shots. However, the calibration charge does not decrease to the same degree while decreasing the voltage during the last 25 shots. The calibration charge is also a bit larger in general in this case, ranging from -0.03 to 0.1 pC. The variance within each voltage level, however, is similar to the measurements with positive plane electrode.

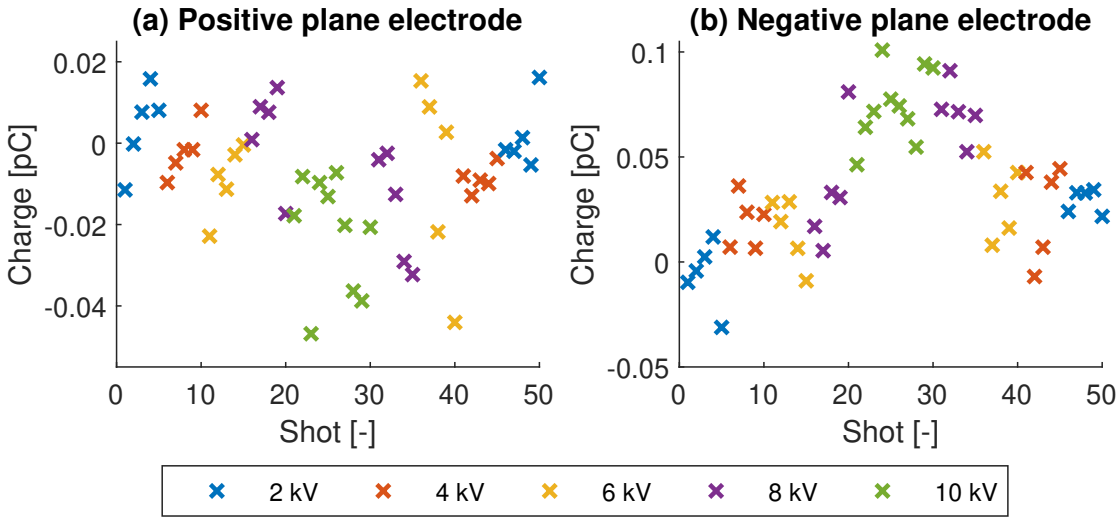

Figure 4.7: Charge subtracted during numerical calibration of the measurements performed with the 2 µm needle electrode

Similarly, the charge subtracted for the measurements with the 6 µm electrode is presented in Figure 4.8. For the measurements with the positive plane electrode, the calibration charge also appears to be increasingly negative with increasing voltage, but there is a large of variance even within the measurements at the same voltage. For example, the calibration charge for the measurements at 10 kV range from -0.05 to 0.30 pC. When the voltage is reduced again, the calibration charge is reduced slightly for the measurements at 4-8 kV, with a more pronounced reduction for the measurements at 2 kV. The calibration charge for the measurements with the negative plane electrode are more consistent, as they are all between -0.1 and +0.1 pC, except for a single outlier at 10 kV. This outlier is the one presented in Figure 4.6.

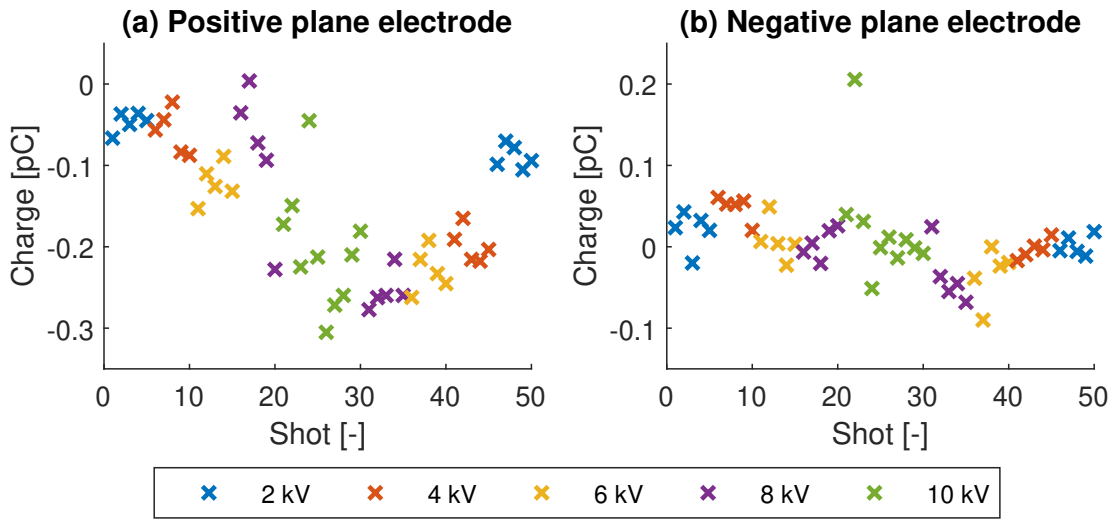

Figure 4.8: Charge subtracted during numerical calibration of the measurements performed with the 6 µm needle electrode

4.3.2 Measurements with 2 µm needle electrode

Positive plane electrode

The individual measurements performed with the 2 µm needle electrode and a positive plane electrode at 5 kV are presented in Figure 4.9. The entire dataset of individual measurements are available in Appendix C, but the measurements at 5 kV are presented here to describe the general trends observed. The individual measurements show very consistent results. However, the noise/signal is quite large, as the measurements are in the range of 0-0.4 pC, and the measurement rapidly oscillates approximately ± 0.05 pC, resulting in a quite broad curve. A larger oscillation is observed every 15 µs, of approximately ± 0.15 pC. There is no systematic relation between the timing of these oscillations and the triggering of the high voltage pulses. The periodic oscillations were observed in all the measurements, even when no voltage was applied, and as their behavior do not differ for the different measurements, they will not be commented further in this chapter.

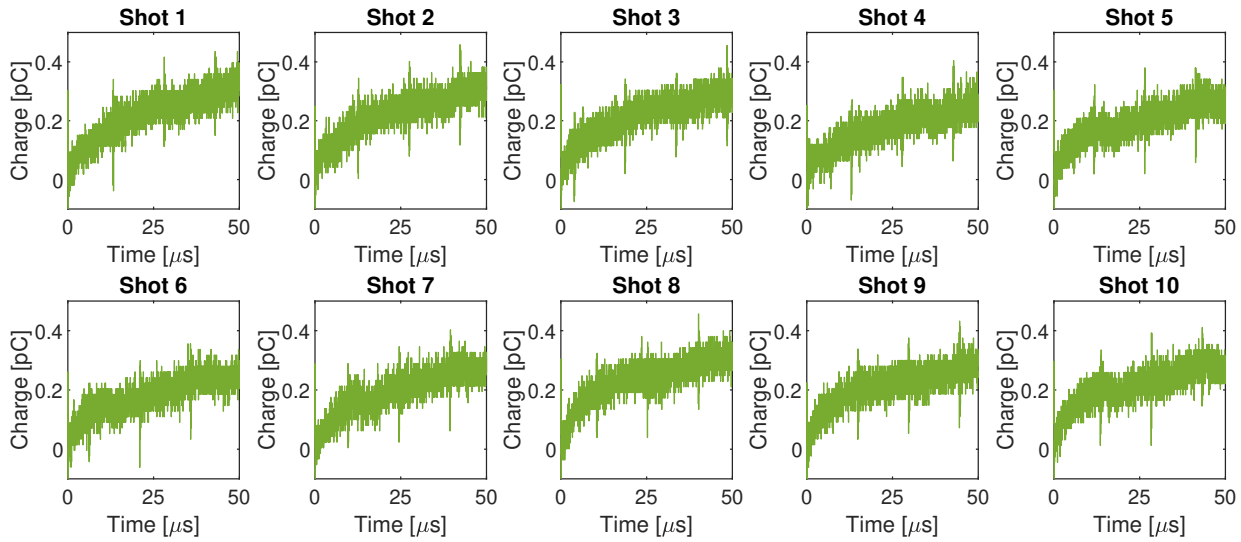

Figure 4.9: Charge measurements with 2 µm electrode and positive plane electrode at 5 kV

In Figure 4.10, the mean value of the first 5 shots (a) and the last 5 shots (b) at each voltage is plotted. In both cases the current is found to increase with increasing voltage. The current is highest during the first part of the pulse, and gradually decreases until the charge measurements display a near constant slope from around 10 µs until the end of the pulse. The first 5 shots and the last 5 shots result in almost identical measurements. The last 5 shots display slightly higher charge at 4 kV and slightly lower charge at 3 kV, but the differences are very small, and there are no noticeable systematical trends.

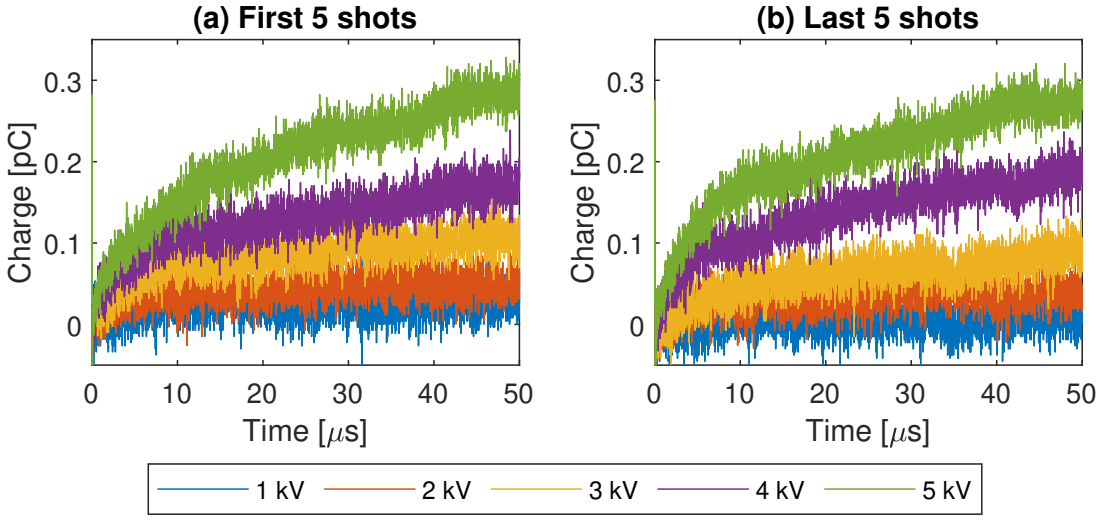

Figure 4.10: Charge measurements performed with 2 µm and a positive plane electrode. Each curve is the mean of the first 5 shots (a) and the last 5 shots (b).

Negative plane electrode

Figure 4.11 shows the charge measurements performed with the 2 µm needle electrode and negative plane electrode. Similarly to the results for the positive plane electrode, these are the mean of the first 5 and last 5 shots, respectively, and the individual measurements are available in Appendix D. The two measurement series give very consistent results, and the current is found to increase with increasing voltage, with a larger gap between each measurement series at the higher voltages. As was observed for the positive plane electrode, the current is highest immediately after the high voltage pulse is initiated, and gradually increases until a steady current is reached from about 10 µs.

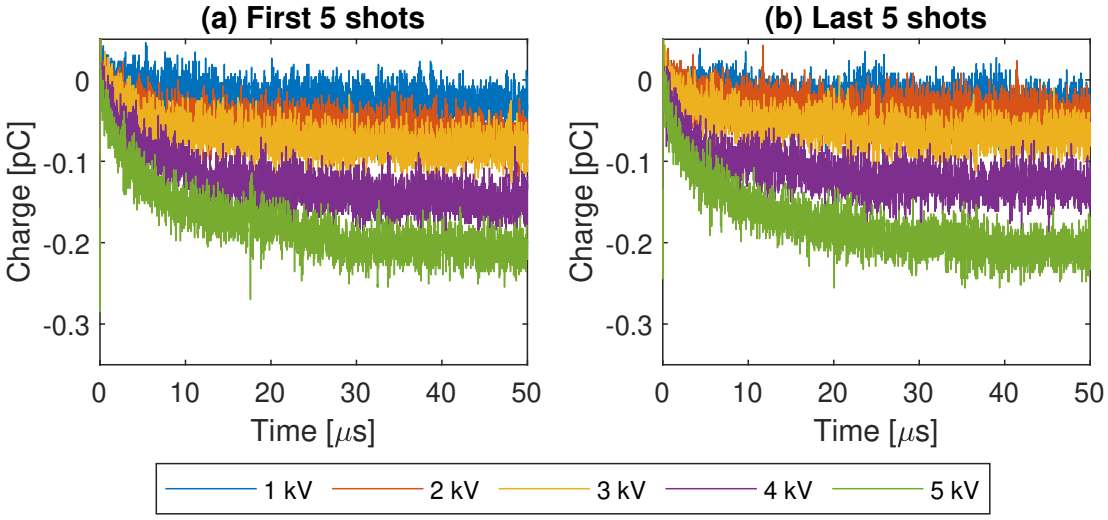

Figure 4.11: Charge measurements performed with 2 µm and a negative plane electrode. Each curve is the mean of the first 5 shots (a) and the last 5 shots (b) performed at each voltage.

Comparison of positive and negative polarity

Figure 4.12 show the mean values of all the shots performed with the 2 µm electrode for positive and negative polarity. The two polarities result in quite similar charge measurements, aside from the obvious sign difference. During the first 10 µs the two polarities show almost exactly the same currents. However, the steady current from 10-50 µs is higher for the positive plane electrode than for the negative plane electrode. For both polarities, the distinction between the measurements at each voltage is clearer for the highest voltages, despite constant voltage intervals.

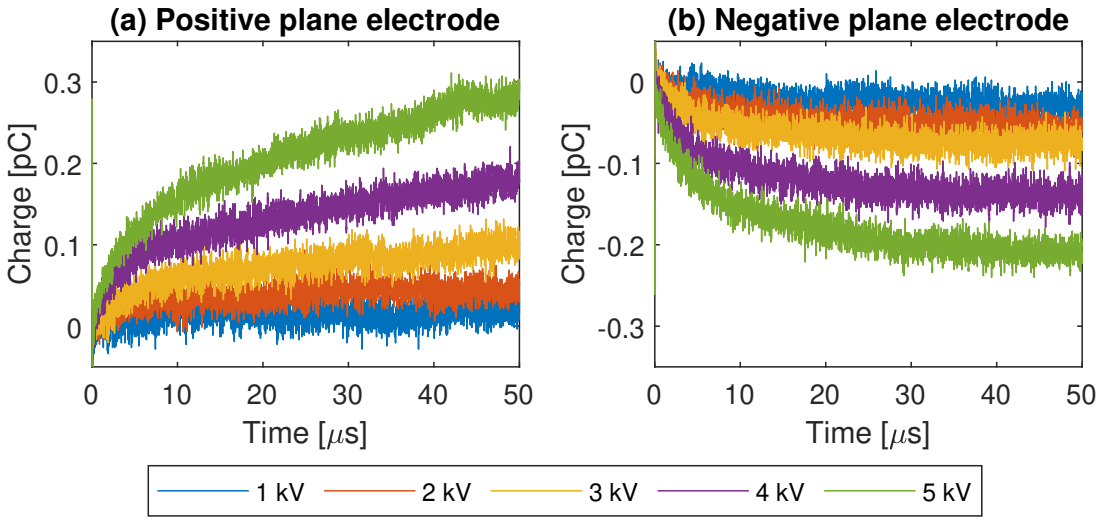

Figure 4.12: Charge measurements performed with 2 µm and both positive and negative plane electrode. Each curve is the mean of the 10 shots performed at each voltage at the given polarity.

4.3.3 Measurements with 6 µm needle electrode

Positive plane electrode

The charge measurements with the 6 µm electrode at positive polarity did not yield consistent results at 10 kV. The individual measurements at 10 kV are presented in Figure 4.13, while the the shots at 2-8 kV are available in Appendix E. For shot 4 and 6 at 10 kV, a sudden sharp increase in the charge is observed shortly after the high voltage is applied, after 0.5 and 1.5 µs respectively. Shot 1, 3, 5, 7, 9 and 10 display a sudden decrease of charge during the high voltage pulses. However, there is no apparent relation between the timing of this decrease relative to the triggering of the pulse.

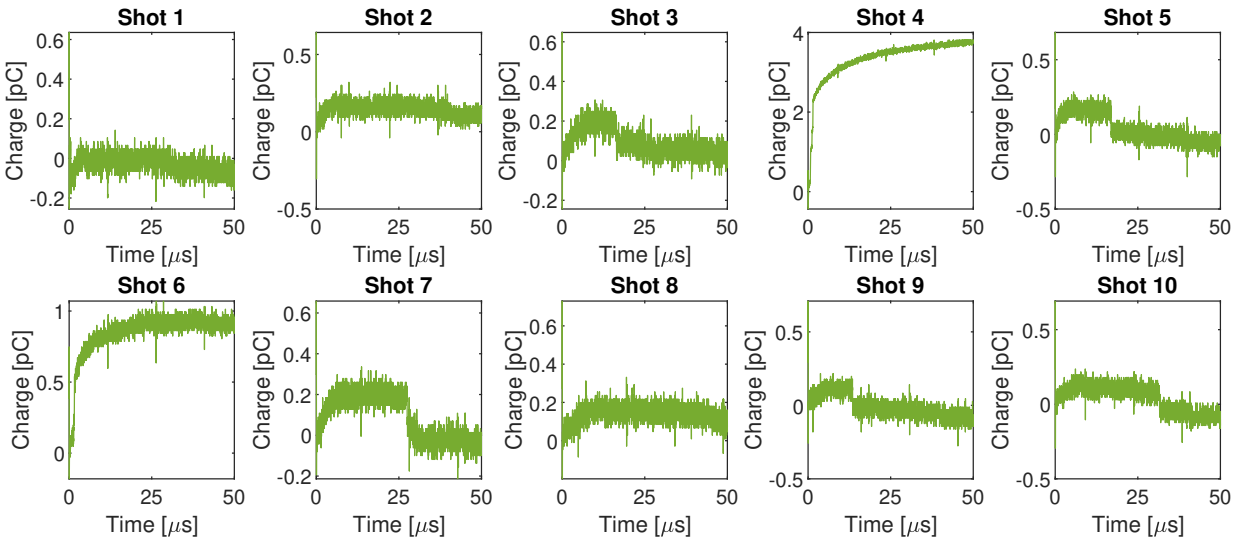

Figure 4.13: Charge measurements with 6 µm electrode and positive plane electrode at 10 kV

The mean charge measured for the pulses of 2-8 kV are presented in Figure 4.14. Shot 2 at 8 kV displayed the same sudden charge decrease which was observed at 10 kV, and was therefore removed from the dataset, but otherwise the measurements gave consistent results. The charge increases with increasing voltage, but the distinction between the measurements at 6 and 8 kV for the first 5 shots (a) is not clear. The last 5 shots (b) display slightly higher charge at 4 kV and 8 kV, than the first 5 shots. The current is highest during the first part of the pulse, and the slope gradually decreases. From about 10 µs and out, the current is very low, and consequentially the curves are horizontal.

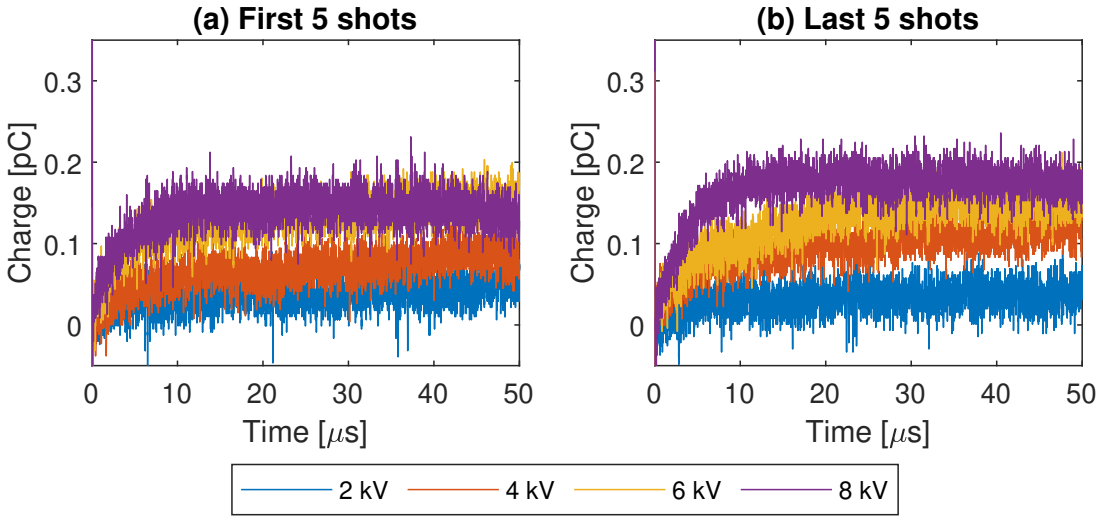

Figure 4.14: Charge measurements performed with 6 µm and a positive plane electrode. Each curve is the mean of the first 5 shots (a) and the last 5 shots (b).

Negative plane electrode

The mean of the charge measurements performed with the 6 µm needle electrode and a negative plane electrode are presented in Figure 4.15, while the individual measurements are available in Appendix F. None of the measurements display the sudden increase in current observed in some of the measurements with a positive plane electrode. However, 5 of the shots at 10 kV, shot 1, 3, 4, 9 and 10, display a sudden drop in charge during the pulse, and have therefore been omitted from the results. All the other voltages yield consistent results, and have been included in the mean values presented in Figure 4.11. The last 5 shots (b) show slightly higher charge at 4 kV, and slightly lower charge at 8 and 10 kV, compared to the first 5 shots (a). Otherwise the results are very similar.

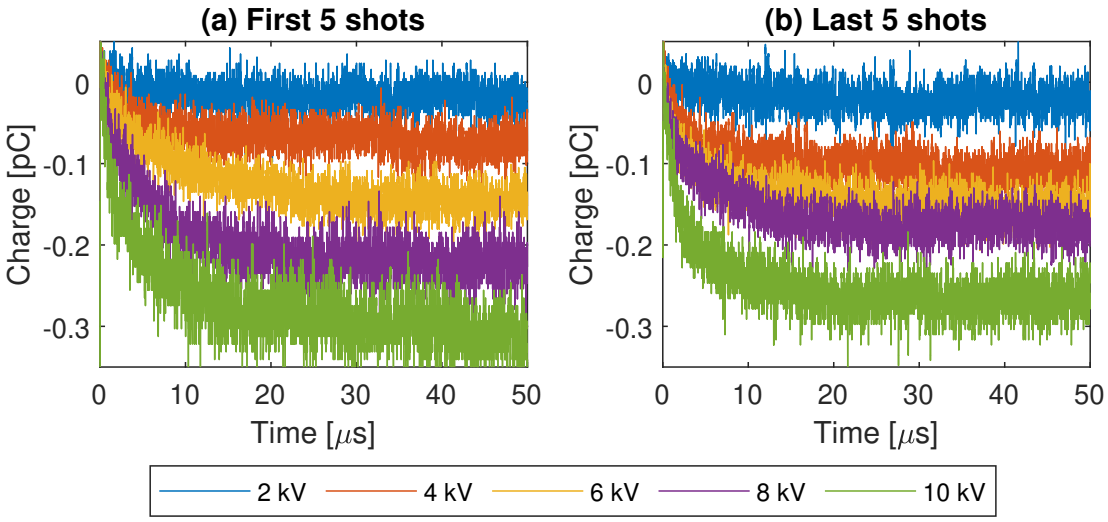

Figure 4.15: Charge measurements performed with 6 µm and a negative plane electrode. Each curve is the mean of the first 5 shots (a) and the last 5 shots (b) performed at each voltage.

Comparison of positive and negative polarity

Figure 4.16 compares the results with 6 µm needle for the two polarities. Apart from the absence of results at 10 kV with the positive plane electrode, there are no notable differences between the two polarities. Unlike the measurements with the 2 µm electrode, the distinction between the charge-curves do not increase with increasing voltage. In fact, there is more overlap between the results at 6 kV and 8 kV, than the results at 2 kV and 4 kV.

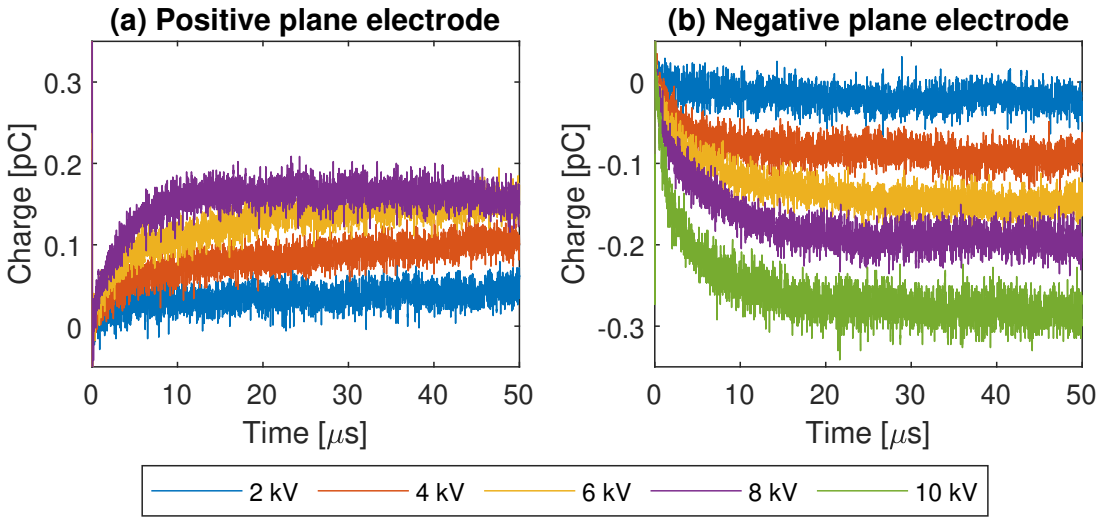

Figure 4.16: Charge measurements performed with 6 µm and both positive and negative plane electrode. Each curve is the mean of the 10 shots performed at each voltage at the given polarity.

4.4 Fitting of numerical model to experimental results

The fitting of the numerical model to the experimental results was an iterative process, and simulations has therefore been performed with a wide range of different parameters. It is not feasible to present every single result from this parameter study in this section. No perfect fit for the experimental results was achieved, as it was found difficult to replicate the behavior of the real system during the entire length of the pulse. This section will present various cases to illustrate the problems experienced during the fitting, and highlight the strengths and weaknesses of the model.

While fitting the numerical model, most of the work has focused on the measurements performed with the 2 µm electrode, as these results were available earlier. The resulting conductivity estimates were then used in simulations with the 6 µm electrode and compared to experimental results, to investigate whether the same conductivity can describe both the datasets.

4.4.1 Fitting the mean current during the first 10 µs

First, the parameters in Equation 2.2 were fitted to replicate the relation between the mean current during the first 10 µs of the pulse, and the applied voltage. This resulted in the following conductivity formula:

$$\sigma(E) = 7.0 \cdot 10^{-9}\,\mathrm{S/m} \cdot \exp\left(5.0 \cdot 10^{-9}\,\mathrm{C/N} \cdot E\right) \tag{4.3}$$

The estimated currents are compared to the experimental results in Figure 4.17. While the mean current during the first 10 µs fits very well, the numerical model greatly overestimates

the current later in the pulse, and the error increases with increasing voltage. The reason for this can be seen in Figure 4.18, which shows the estimated charge profiles, as the numerical model does not match the the time dependence of the current observed in the experimental measurements. Instead of the current being high in the beginning of the pulse, and gradually decreasing, the current is almost constant during the entire length of the pulse. This behavior was observed for any simulations performed with the pre-exponential factor $\sigma_0 \geq 2 \cdot 10^{-9}$ S/m and $n = 1$. However, no good fit for the mean current during the first 10 µs was achieved for smaller values of σ_0. For other n-values, the "linear limit" for the pre-exponential factor changes, but the general trends are the same. None of the simulations succeeded in replicating both the sharp charge increase immediately after the pulse was applied, while also flattening out to the extent that the experimental results do.

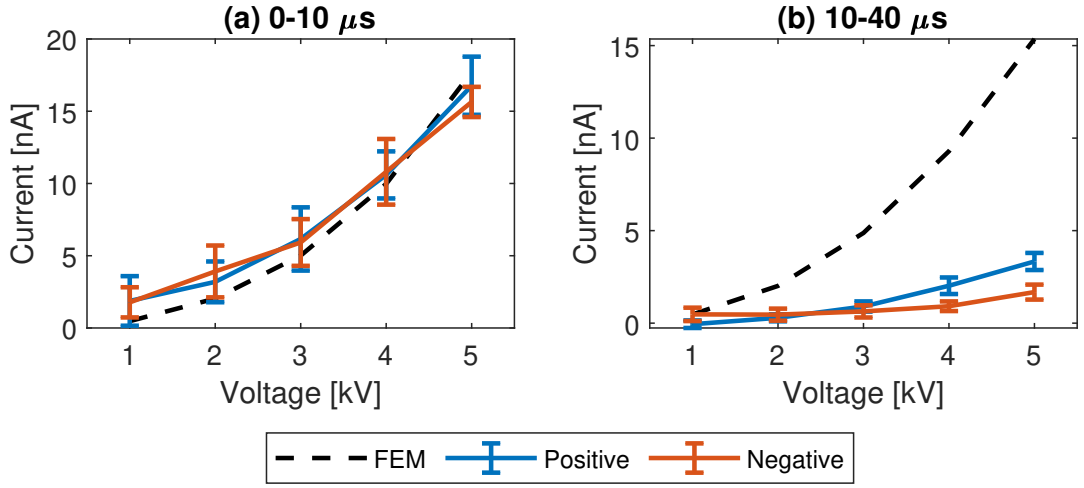

Figure 4.17: Mean current during the first 10 µs and from 10 to 40 µs calculated with the numerical model (FEM), and measured during experiments with a 2 µm needle electrode. The conductivity formula used for numerical modelling is presented in Equation 4.3, and the polarity refers to the sign of the plane electrode. The error bars correspond to the standard deviation of the experimental results.

The conductivity of Equation 4.3 was also used for simulations with the 6 µm needle electrode. In Figure 4.19, these numerical results are compared to the corresponding experimental results, by comparing the mean currents. The numerical model is found to both overestimate the current during the first 10 µs for voltages above 6 kV, as well as greatly overestimating the current later in the pulse.

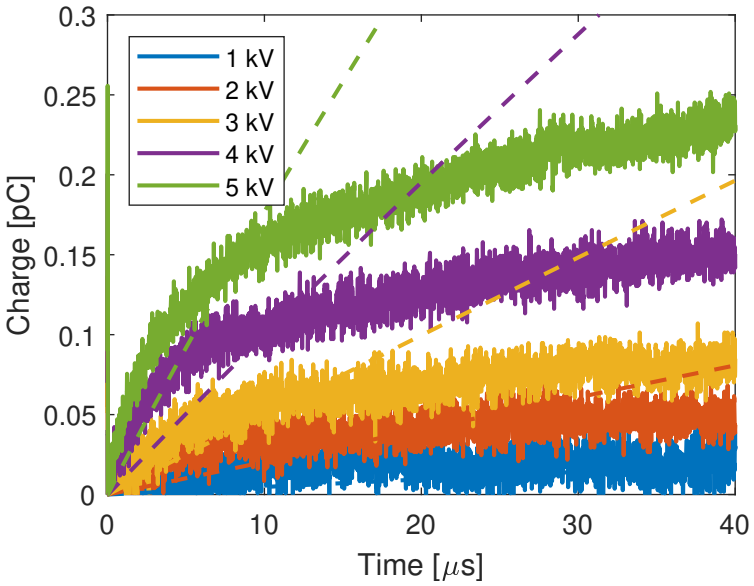

Figure 4.18: Mean values of charge measurements performed with 2 µm electrode (solid lines) and results from numerical modelling with conductivity formula described in Equation 4.3 (dashed lines).

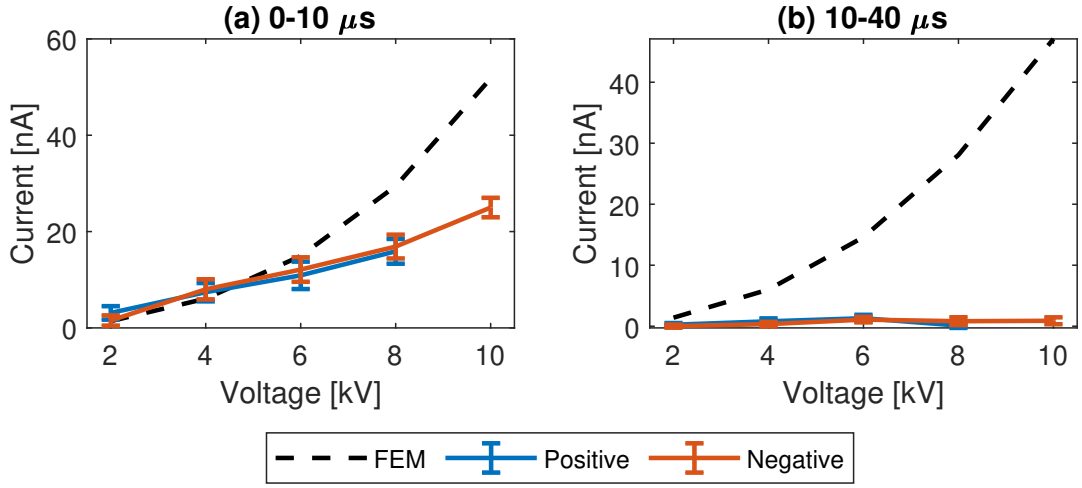

Figure 4.19: Mean current during the first 10 µs and from 10 to 40 µs calculated with the numerical model (FEM) and measured during experiments with a 6 µm needle electrode. The conductivity formula used for numerical modelling is presented in Equation 4.3, and the polarity refers to the sign of the plane electrode. The error bars correspond to the standard deviation of the experimental results.

4.4.2 Fitting the mean current from 10 to 40 µs

Further attempts at fitting the numerical model focused on fitting the mean current from 10 to 40 µs measured with the 2 µm electrode. There were some differences between the

measurements with the positive and negative plane electrode, but to simplify the fitting procedure, the fitting focused on the measurements with a positive plane electrode. Fitting the mean current from 10 to 40 µs resulted in a conductivity of:

$$\sigma(E) = 1.0 \cdot 10^{-10}\,\mathrm{S/m} \cdot \exp\left(1.6 \cdot 10^{-8}\,\mathrm{C/N} \cdot E\right) \tag{4.4}$$

When comparing this equation to Equation 4.3, presented in the previous section, the pre-exponential factor σ_0 is significantly smaller in this case ($1.0 \cdot 10^{-10}$ vs. $7.0 \cdot 10^{-9} S/m$).

The estimated currents are compared to the experimental results in Figure 4.20. The mean current from 10 to 40 µs fits well with the measurements with the positive plane electrode. The numerical model shows slightly higher currents at 5 kV, but this is still within the standard deviation of the experimental results. For the first 10 µs, however, the numerical model underestimates the current. The model predicts almost no current at 1 and 2 kV, but the current increases with increasing voltage. In fact, the slope of the current/voltage curve is steeper for the numerical model than for the experimental results at higher voltages. This causes the mean current the first 10 µs at 5 kV to be very similar for the numerical and experimental results.

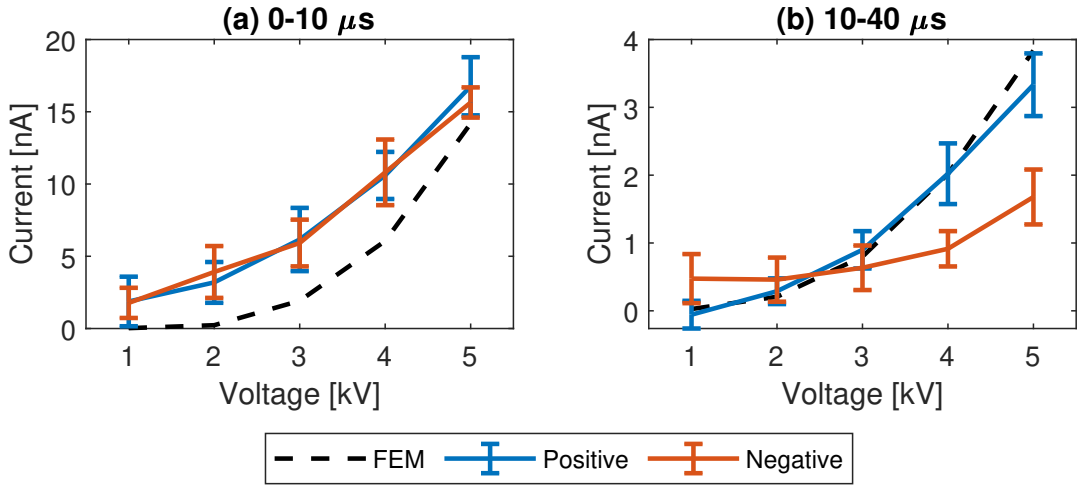

Figure 4.20: Mean current during the first 10 µs and from 10 to 40 µs calculated with the numerical model (FEM), and measured during experiments with a 2 µm needle electrode electrode. The conductivity formula used for numerical modelling is presented in Equation 4.4. The error bars correspond to the standard deviation of the experimental results.

Figure 4.21 compares the estimated charge profiles with the experimental results performed with the 2 µm electrode. The shape of the charge/time curves matches the experimental results better in this case, showing a higher current in the beginning of the pulse that gradually decreases until at more or less stable current is reached. However, the underestimation of the current the first few microseconds, described in the previous paragraph, does cause some deviance between numerical and experimental results below 5 kV.

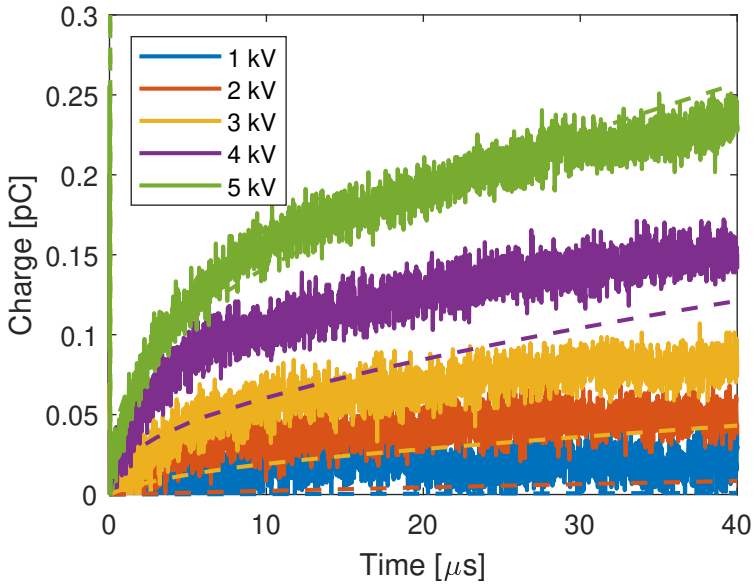

Figure 4.21: Mean values of charge measurements performed with 2 µm electrode (solid lines) and results from numerical modelling with conductivity formula described in Equation 4.3 (dashed lines).

Numerical simulations were also performed with Equation 4.4 and the 6 µm electrode. The resulting mean currents are compared to the experimental results in Figure 4.22. In this case, the numerical results do not fit either the first 10 µs or from 10 to 40 µs. The numerical model predicts the current to increase exponentially with applied voltage, while the experimental results show a linear relation between current and voltage.

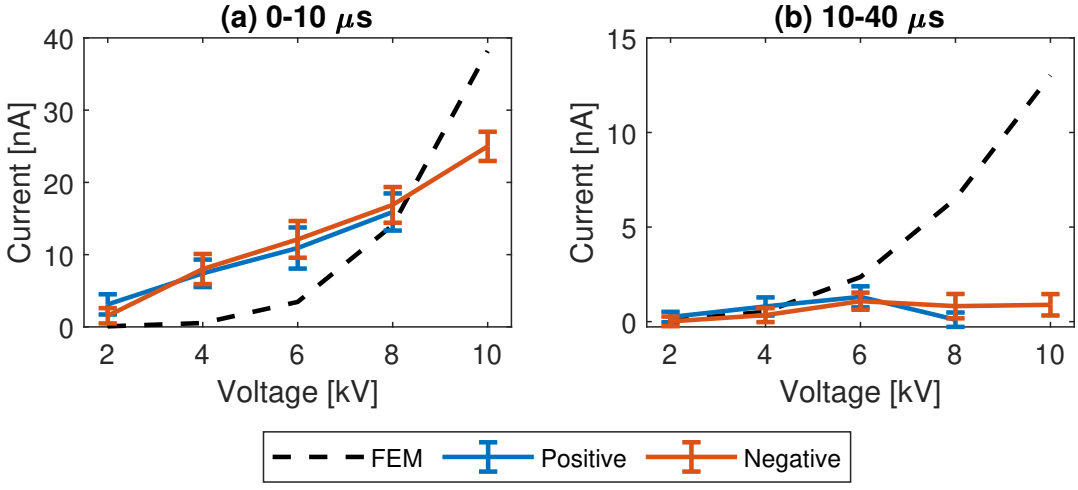

Figure 4.22: Mean current during the first 10 µs and from 10 to 40 µs calculated with the numerical model (FEM) and measured during experiments with a 6 µm needle electrode and positive/negative plane electrode. The conductivity formula used for numerical modelling is presented in Equation 4.4. The error bars correspond to the standard deviation of the experimental results.

4.4.3 The effect of the rise time on numerical results

While all of the simulations were performed with a rise time of 50 ns, the rise times observed in the experiments varied, depending on the applied voltage, from 40 to 60 ns. To investigate whether this could be a source of error while comparing numerical and experimental results, simulations were run with the conductivity of Equation 4.4 and the 2 µm electrode, with varying rise times. The resulting charge profiles are presented in Figure 4.23, together with the experimental results. These results show that the currents estimated by the numerical model do not change significantly by changing the rise time of the pulse

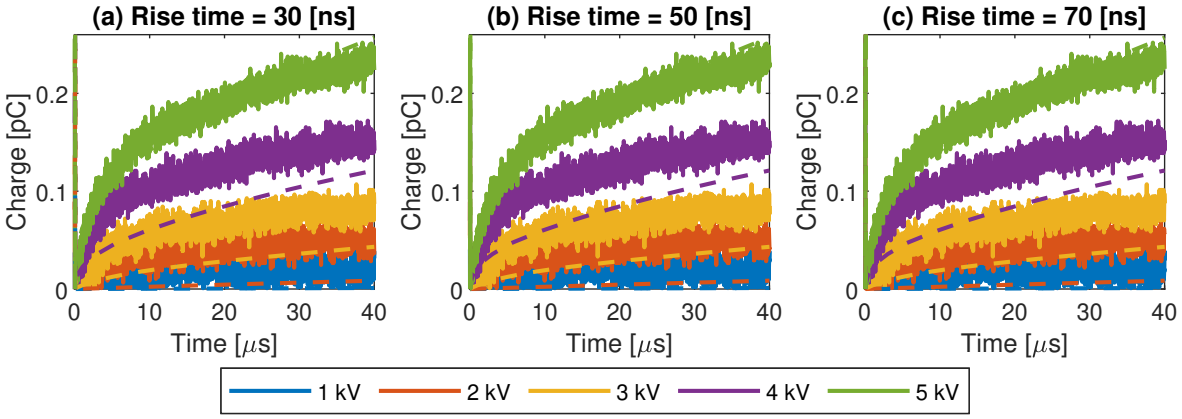

Figure 4.23: Mean values of charge measurements performed with 2 µm electrode (solid lines) and results from numerical modelling with conductivity formula described in Equation 4.3 (dashed lines), with varying rise times.

Chapter 5

Discussion

5.1 Accuracy and reliability of charge measurements

The currents measured in these experiments are very small, which makes it very hard to get accurate measurements. To ensure precise measurements, a lot of effort was put into limit the effects of external noise, by avoiding ground loops in the system and mounting ferrite cores around connecting cables. The setup was also carefully calibrated to limit contributions from the displacement current to the total current. While there were still some noise and displacement current present in the final measurements, the results achieved in these experiments are generally very consistent.

5.1.1 Noise

To illustrate the precision required, one can consider the highest sensitivity possible to achieve with the oscilloscope and measurement capacitors used in these experiments. The oscilloscope, a Tektronixs TDS 540, has a maximum resolution of 1 mV/division, with 25 digitizing levels per division [30]. When combined with the 472 pC measurement capacitors, this results in a charge sensitivity of approximately 0.02 pC. This is very close to the charge measured for the lowest voltages, particularly the measurements at 1 kV with the 2 µm electrode. Even for the highest voltages, the charge is only around 0.3 pC at its peak, which is only 15 times the minimum measurable charge. In practice, the individual charge measurements rapidly oscillate $\pm$ 0.05 pC, making it difficult pinpoint the exact charge at any given time. This results in a quite broad curve with a width of approximately 0.1 pC, as shown in Figure 4.9 and 4.13. The cause for this charge-broadening is not known. Multiple shots were therefore performed at each voltage, and the mean value of these shots was used to better differentiate between the measurements at different voltages.

There also appears to be some periodic noise that affects the measurements, as a larger oscillation is observed every 15 µs. The source of this noise was not successfully located, and it was present even when no voltage was applied. However, these periodic pulses were not observed

in the voltage measurements from the capacitive probe, indicating that this originates from the differential amplifier or the connections surrounding it. Assuming the noise is caused by ambient electromagnetic radiation, the period of the noise corresponds to a frequency of 67 kHz. This does not match with the frequencies used in Norway for radio broadcasting (87.5 -240 MHz), television broadcasting (470 - 694 MHz), mobile communication (738 - 27 500 MHz) or WiFi networks (2.4 and 5.0 GHz) [31]. While it is unfortunate that the cause for the periodic noise has not been identified, the noise does not significantly alter the results, as the trends of the charge measurements are still easily distinguishable.

5.1.2 Calibration of charge measurements

The initial jump in the charge measurements, described in Section 4.3.1, is likely caused by displacement currents. This behavior is similar to what is observed before the height of the electrodes is calibrated properly, even though the setup was carefully calibrated before the measurements were started. There are two separate characteristics of this displacement that should be evaluated. The first is that the absolute value of the initial jump generally seems to increase with increasing voltage, and the second is that there is quite a lot of variance even for the measurements at the same voltage. This large variance does make the systematic increase of calibration charge with increasing voltage less clear, but because it is observed to at least some degree for at least 3 of the 4 cases (it is not clear for the measurements with the 6 µm electrode and negative plane electrode), there does seem to be a pretty clear trend.

The increasing initial jump with increasing voltage likely has a quite simple explanation. As the setup was calibrated at low voltage, the resulting displacement currents will be quite small. Consequentially, there might be a small error in the calibration that is practically invisible at low voltages, but is more apparent at high voltages. Because the setup was calibrated before each measurement series, the extent of this voltage-dependent calibration voltage can easily be slightly different for each dataset. This behavior is observed in the results, as the calibration charge is higher for the negative plane electrode for the 2 µm-measurements, while the measurements with the 6 µm electrode exhibit higher calibration charge at negative polarity. However, if this was only cause for these displacement currents, the calibration charge would simply increase linearly with the applied voltage, and remain constant at each voltage level.

This does not match the behavior observed in Figure 4.7 and 4.8, as the calibration charge is found to vary greatly even within each voltage level. Over time, the position of the electrodes was found to change slightly, and to account for this, the setup was calibrated before each measurement series was started. As the measurement series were quite long, approximately 40 hours, there could be some displacement of the electrodes during the measurements as well. The high voltage pulses may also directly cause some electrode displacement, as hydrodynamic currents in the cyclohexane may push the electrodes slightly. As described previously, the charge measurements constantly oscillates $\pm$ 0.05 pC, which makes it difficult to pinpoint the charge at any given time, and correspondingly introduces some more variance to

the calibration charge.

The variance of the calibration charge was particularly large for the measurements with the 6 µm electrode and a positive plane electrode. Notably, the variance within each voltage level is considerably higher than for the corresponding measurements with a negative plane electrode. As the electrodes were not removed from the cell between these measurements, their mounting within the electrode holders should not differ between the two cases. There were, however, some other problems with the measurements at high voltage for the measurements at positive polarity, which might be related to this large variance. These will be discussed in the next subsection. For the measurements at negative polarity the calibration charge is much more stable, outside of the shot 2 at 10 kV. It is unclear why this specific shot is so different from the other measurements. However, as this measurement is otherwise consistent with the other results, it is still included in the overall results.

When the pulse is triggered there are also some rapid changes initially, first a dip and then a sharp increase, before the charge stabilizes, as shown in Figure 4.6. As these fast fluctuations do not match the expected behavior of the system, they were most likely caused by defects in the measurement setup, rather than representing actual currents in the system. While the details of why this happen is not known, it is not unlikely for rapidly changing voltages during the measurements to induce some sort of response elsewhere in the setup. These fluctuations were therefore not considered when numerically calibrating the charge.

The behavior of the charge measurements during the initiation of the pulse and the variance for the calibration charge show how delicate these measurements are. Even though the setup was calibrated before the measurements started, the initial displacement currents were often at the same scale as the conduction currents that were measured. Numerical calibration was therefore clearly necessary to get accurate measurements of the conduction currents. There is always a risk when manipulating the measurement data, as some of the contributions from the conduction may be accidentally subtracted from the results. However, as there is a quite large distinction between the rapid fluctuations as the pulse is applied and the more gradual changes afterwards, the confidence in the numerical calibration is quite high. The measurements also show very consistent results after the numerical calibration. Because of this, the numerical calibration of the results appears to be successful.

5.1.3 Discharges and other phenomena at very high voltage

Some irregular behavior was observed at 8 and 10 kV for the measurements with the 6 µm electrode. As shown in Figure 4.13, two of the shots with positive plane electrode at 10 kV displayed a sharp increase in current shortly after the pulse was applied. A more widespread issue was the sudden drop in the charge observed in many of the measurements. This was observed for 1 measurement at 8 kV and 6 measurements at 10 kV with positive plane electrode, as well as 5 measurements at 10 kV with negative plane electrode.

The sudden increase in current observed at 10 kV with positive plane electrode is likely a consequence of discharges through the cycloehxane. This behavior matches the expected be-

havior of discharges. The previously reported inception voltage of streamers in cyclohexane, presented in Figure 2.2, estimate an inception voltage of 13 kV for positive streamers. However, as negative streamers typically have a lower inception voltage than positive streamers, the measurements performed with positive plane electrode are likely very close to the corresponding inception voltage. This explains why these discharges are only observed for the measurements with the plane electrode at positive polarity.

While the discharges make it difficult to do further analysis of some of the measurements, they do not appear to have a lasting effect on the system. The 6 µm needle electrode is not changed at all during the discharges, as shown by the SEM-images in Figure 4.2. The 2 µm electrode was also exposed to discharges, as high voltage pulses were accidentally applied while the cell was empty, and this doesn't appear to have damaged the needle either. The 40 minute delay between each shot is also quite long and should be sufficient to let the cyclohexane self-heal before the next shot. For comparison, inception of streamers in cyclohexane has previously been investigated with only 15 minutes of delay between each shot [15, 21]. Nonetheless, there was quite high variance for the calibration charge of the measurements at 10 kV with positive plane electrode, and the calibration charges of the measurements with discharges, shot 4 and 6, are respectively the lowest and highest among these measurements. However, there it is not clear why this would be the case, as any lasting changes caused by the discharges would be observed for the measurements following the discharges. While there were some problems with these measurements, the following measurements at decreasing voltage show consistent behavior, and have been included in the overall results.

The reason for the sudden drop in the charge measurements for many of the shots at 8 and 10 kV is not known. No previous record of this behavior was found, and it is not clear whether this represents the behavior of the system itself, or if it is a defect of the measurement setup. This does introduce some uncertainty whether the experimental setup works completely as intended, but as the other measurements show consistent, regular behavior, these irregular measurements have simply been removed from the dataset before further analysis have been performed.

An unfortunate side effect of the problems at high voltage is the low sample size for the measurements at 10 kV. In total, 8/10 of the measurements with positive plane electrode and 5/10 of the measurement with negative plane electrode were deemed unusable, and were not included in the presentation of the mean values. For the measurement with the positive plane electrode, the sample size of 2 shots is so low that the results were scrapped entirely. While the the other 5 shots with negative plane electrode were still included in the presentation of the results, there is increased uncertainty for these results due to the small sample size.

5.1.4 Consistency of the measurements

As discussed earlier, these are very sensitive measurements, and very small changes system can lead to significant errors. Because of this, the 10 shots applied at each voltage were split into two series of 5 shots, so that these two series could be compared to each other. As the first 5 shots per voltage were performed while increasing the voltage, followed immediately

by 5 shots per voltage while decreasing the voltage, the time delay between the two measurement series is longest for the measurements at the lowest voltages and shortest for the measurements at the highest voltages. Consequentially, if the system is somehow gradually changed during the measurement cycle, it would be most apparent for the measurements at the lowest voltages.

Figure 5.1 compares the mean current of first 5 shots and last 5 shots applied at each voltage for the 2 µm electrode. These figures show that while mean of the first 5 and last 5 shots display slightly different mean values, the means are almost always within the standard deviation of each other, with the exception of the measurements with the negative plane electrode at 2 kV. However, in both cases the first 5 shots quite systematically display slightly higher currents than the last 5 shots. It might have been beneficial to perform more measurements at each voltage, to investigate whether this is a coincidence due to the variance of the measurements, or represent actual changes of the system.

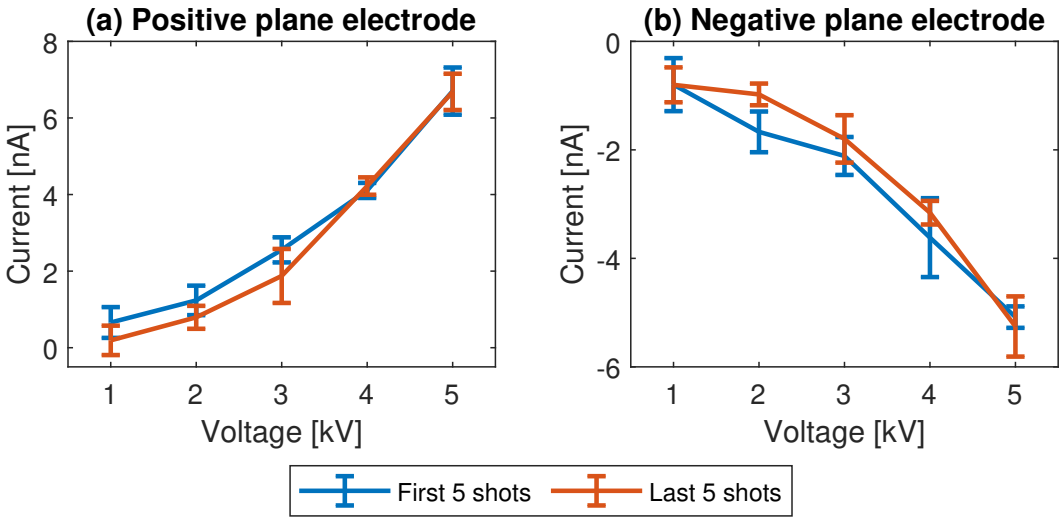

Figure 5.1: Mean current during the first 40 µs of the pulse for the measurements with the 2 µm electrode and positive (a) and negative (b) plane electrode. Each plot compares the mean values for the first 5 shots and the last 5 shots for each polarity, with the standard deviation presented as error bars.

One reason why the currents might decrease during the measurements is polymerization of cyclohexane on the surface of the needle electrode. The SEM images of the 2 µm needle electrode after the experiments show that some contamination has deposited on the surface, which could reduce the measured currents. If this contamination got deposited during the measurements, for example as a consequence of electropolymerization of cyclohexane at high voltages, it would explain why the later measurements display lower currents. However, it's more likely that the contamination has been present during all the measurements. The 6 µm electrode was exposed to even higher voltages, but was completely clean after the experiments. As the main operational difference between the two electrodes was the time it was stored in the test cell, 101 days for the 2 µm and 24 days for the 6 µm electrode, the contamination has

probably been deposited during the time before the measurements started. Because of this, the very slight differences between the first and second measurement series are most likely a consequence of the statistical variance of the results.

The measurements with the 6 µm electrode also give very consistent results, as shown by the mean currents presented in Figure 5.2. the first 5 shots show slightly lower currents at 4 and 8 kV with positive plane electrode, but it is not statistically significant. The standard deviation for the measurements with the 6 µm and positive plane electrode are also generally a bit higher than for the other measurement series. With negative plane electrode, the current measured at 4 kV is slightly higher for the last 5 shots, but as this is not observed at any of the other measurements, it is likely coincidental.

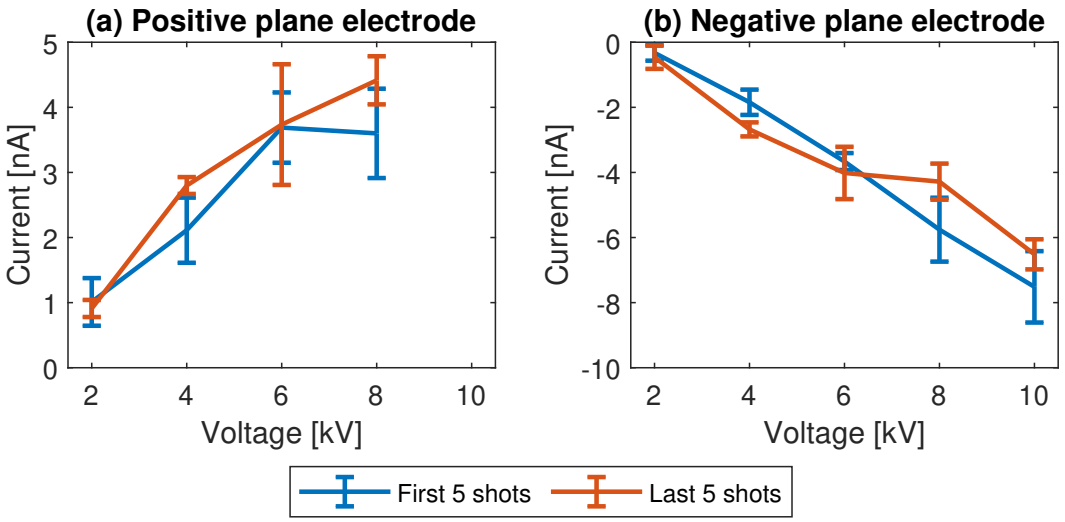

Figure 5.2: Mean current during the first 40 µs of the pulse for the measurements with the 6 µm electrode and positive (a) and negative (b) plane electrode. Each plot compares the mean values for the first 5 shots and the last 5 shots for each polarity, with the standard deviation presented as error bars.

Overall the measurements give very consistent results. There are some differences, but this is probably due to statistical variance. While 10 shots per voltage does appear to give accurate results, increasing the sample size could reduce the uncertainty further. This would be especially beneficial for the measurements at low voltage, where the noise/signal-ratio is particularly high. In future works, more measurements could be performed at low voltage, without unnecessarily stressing the system further at high voltage. However, the sample size used in this work does result in consistent results, despite the amount of noise present in the measurements.

5.2 Characteristics of the charge measurements

In this section the characteristics of the charge measurements will be discussed, and the influence of the polarity and tip radius will be evaluated. This will be linked to the known theory for high field conductivity in dielectrics. All the charge measurements performed in the experimental work show a similar charge/time-profile. The current is highest during the initiation of the high voltage pulses, then it gradually decreases until it reaches a steady current from approximately 10 µs. This behavior is consistent with the theory for space charge limited fields, which was presented in Section 2.3. As the high voltage is applied, the field around the tip of the needle quickly increases, resulting in increased conductivity. Further away from the needle the field, and correspondingly the conductivity, is much lower, resulting in an accumulation of charge. This redistribution of charge reduces the overall field, and correspondingly the current is reduced. After a while a steady state condition is reached, where there is very low net-movement of charge, and the charge distribution in the cyclohexane is nearly constant. The steady current may therefore be described as a *space charge limited current*.

5.2.1 Influence of electrode polarity

Figure 5.3 compares the currents with positive and negative plane electrode for the measurements with the 2 µm electrode. The current during the first 10 µs is exactly the same for the polarities, but the steady current later in the pulse is higher for the measurements with positive plane electrode. A possible reason for the higher currents at positive polarity is electron injection from the needle electrode, as charge carrier injection is usually most apparent when the needle electrode is at negative polarity [14]. However the effect of charge injection would not necessarily be expected to increase during the pulse, and does not explain why the currents only are different after the first 10 µs. It is possible that contributions from charge injection are simply overshadowed by other more dominant mechanisms during the first few microseconds, as the current in the beginning is relatively large. Later in the pulse, when the overall current is decreased, the contributions of charge injection become more apparent.

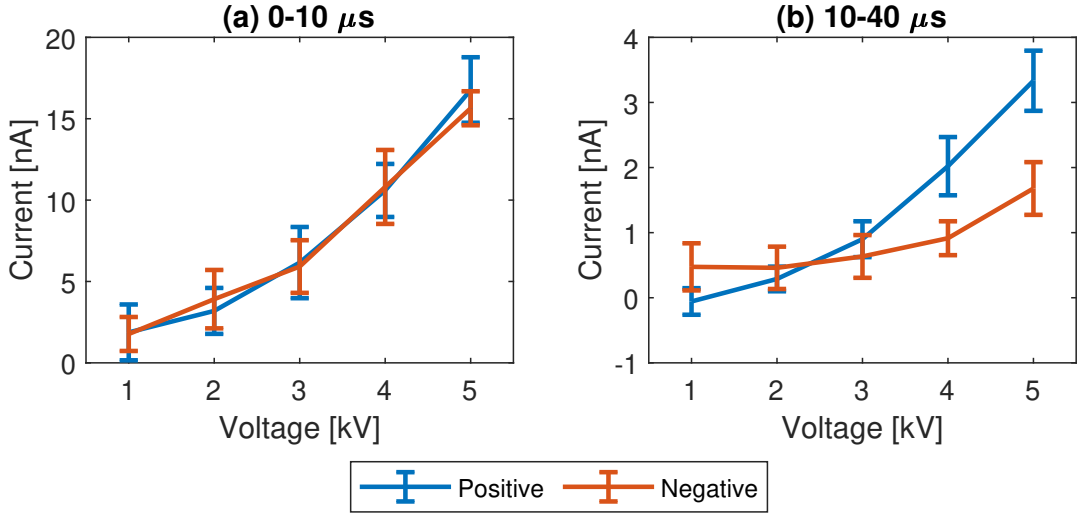

Figure 5.3: Mean current during the first 10 µs (a) and between 10-40 µs (b) of the pulse for the measurements with the 2 µm needle electrode. The standard deviation is presented as error bars, and the polarity refers to the polarity of the plane electrode.

The measurements with the 6 µm electrode, on the other hand, do not show a clear relation between the electrode polarity and current. The mean current of the measurements with the 6 µm electrode at positive and negative polarity is presented in Figure 5.4. For the first 10 µs, the two polarities result in very similar currents, and there is also no apparent difference later in the pulse. However, the currents from 10 to 40 µs are very small in this case, so it would be difficult to observe any meaningful difference. To illustrate this; a current of 1 nA over 30 µs, corresponding to the current at 10 kV with negative plane electrode, results in a charge difference of 0.03 pC. This is such a small charge difference that it is almost impossible to measure accurately with the equipment used in this work.

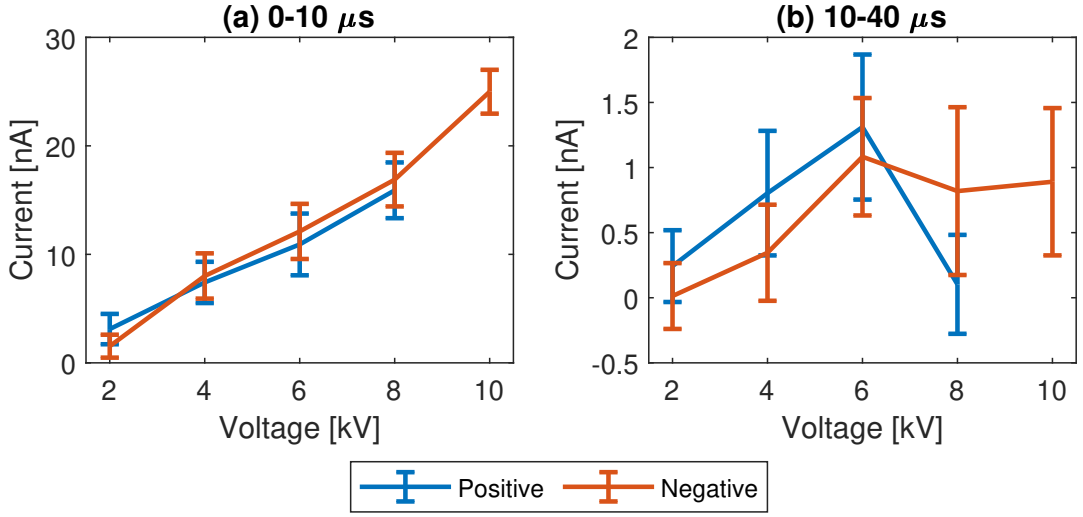

Figure 5.4: Mean current during the first 10 µs (a) and between 10-40 µs (b) of the pulse for the measurements with the 6 µm needle electrode. The standard deviation is presented as error bars, and the polarity refers to the polarity of the plane electrode.

5.2.2 Influence of electrode tip radius

The mean current during the first 40 µs of the pulses is compared for the two electrodes in Figure 5.5. While the voltages applied in each case are different, some trends can still be observed. For the 6 µm electrode, the current increases more or less linearly with increasing voltage, while the slope of the 2 µm-curve increases with increasing voltage. Because of this, the difference between the two electrodes is most apparent at high voltages. The higher currents measured with 2 µm electrode are a consequence of the sharper tip curvature, which results in higher electric fields near the tip of the needle. As the conductivity of cyclohexane increases with increasing electric field, the measurements with the 2 µm electrode results in higher currents than the measurements with the 6 µm electrode, even when the applied voltage is the same.

It is interesting, however, that the currents measured with the 6 µm electrode increase linearly with increasing voltage. This is similar to how the mean current through an ohmic material would vary with increasing voltage, but the shape of the charge/time-profiles show that the cyclohexane does not actually behave like an ohmic material. The currents are clearly limited by the redistribution of charge within the liquid, as described in Section 5.2. When comparing the currents during the first 10 µs and from 10 to 40 µs, presented in Figure 5.3 and 5.4, it is clear that while the initial currents are higher for the measurements with the 6 µm electrode, the steady currents afterwards are higher for the 2 µm electrode. This indicates that the space charge limited region is smaller. The steady current is therefore lower for the measurements with the 6 µm needle, despite the higher voltages.

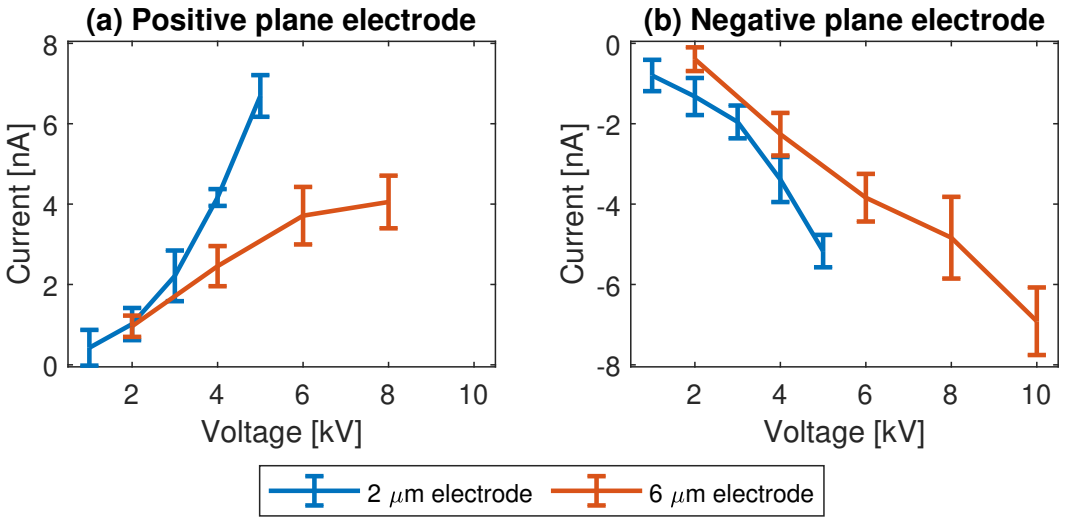

Figure 5.5: Mean current during the first 40 µs of the pulse for the measurements with positive (a) and negative (b) plane electrode. The standard deviation is presented as error bars.

5.2.3 Comparison to previous results

The charge measurements performed in this work show significantly smaller currents than result previously reported by the author. For measurements with a 2 µm needle electrode and positive plane electrode, there was previously observed mean currents up to 75 nA at 5 kV [15]. Under similar conditions, the measurements in this work display currents of less than 7 nA. This is most likely a consequence of the purity of the cyclohexane. The cyclohexane used in the previous experiment had been stored for a long time, and the container had been opened at closed several times. This may have allowed for contamination to enter the bottle. These contaminants can act as dopants in the system, as explained in Section 2.1.1, which increases the conductivity. For this work, a new bottle was used, and it is therefore more likely to maintain the purity promised by the supplier. The large discrepancy between the two results show that contamination of the system can increase the conductivity of the cyclohexane drastically, and the small currents measured in this work show that the cyclohexane is very pure.

5.3 Accuracy of numerical model

5.3.1 Parameters for numerical modelling

When comparing experimental and numerical results, it is important that the conditions are identical, to achieve comparable results. If the parameters used during numerical modelling are different from the real system, it might lead to systematical errors. In this section some of the factors that could have skewed the comparisons of experimental and numerical results will be discussed briefly.

As the rise time of the pulses was found to increase slightly with increasing voltage, while all the numerical simulations were performed with 50 ns rise time, this could possibly introduce some errors. However, as shown in Section 4.4.3, the numerical modelling is found to be nearly independent of the rise time, at least for the range of rise times observed in these experiments. Because of this, the varying rise time is unlikely to have caused any major errors during fitting of the numerical model.

There could also be a slight mismatch between the height of the needle electrode in the experiments, and the height used in the numerical model. The height of the needle was measured by external inspection using binoculars mounted on an adjustable stand, so there could potentially be some errors due to refraction. The refractive index of cyclohexane is 1.42 [32], which is slightly higher than water. However, this is unlikely to have significant effect on the results, as the incident angle is low and the influence of the needle-plane distance has found to be very small for distances around 7 mm [24].

The contamination present on the surface of the 2 µm electrode after the experiments may have reduced the induced currents compared to the ideal scenario with a clean needle. As discussed previously, the contamination has probably been deposited before the measurements started, and has been present for all the measurements performed with this needle. This could lead to the numerical model overestimating the currents compared to the experimental results.

5.3.2 Strengths and weaknesses of the numerical model

While a perfect fit for the experimental results was not achieved, the numerical simulations with a simple field dependent electrical conductivity do replicate some of the characteristics of the experimental measurements. The simulations performed with the conductivity given by Equation 4.4, which was fitted to the current from 10 to 40 µs, display the same sharp increase as the pulse is initiated, followed by decreasing current until a steady current is established. However, it was found difficult to fit how the initial current increases with increasing voltage, while at the same time replicating the comparatively low steady current. The conductivity fitted to the measurements with the 2 µm electrode also failed to accurately predict the measurements with the 6 µm electrode. Consequentially, the numerical model used in this work is not found to adequately describe the real system.

To fit the initial current of the pulse at all the voltages, the pre-exponential factor σ_0 had to be quite high compared to the previously reported conductivity. However, this conductivity model, presented in Equation 4.3, fails to replicate the shape of the experimental measurements, as the charge increased more or less with increasing time during the pulse. This pre-exponential factor corresponds to the conductivity of cyclohexane at zero field. If conductivity of the cyclohexane outside of the high field region is too high to effectively limit the movement of charges, the space charge will build up more slowly, and only at very high voltages. This is confirmed by the estimated field at the tip of the 2 µm during numerical simulations, which is presented in Figure 5.6. In the case of high conductivity at zero field, presented in Figure 5.6a, the field is only significantly limited by space charge at 4 and 5 kV,

and even then it takes a relatively long for the space charge limited field to establish itself. This is compared to the case with lower conductivity at zero field in Figure 5.6b, which flatten out to a steady current similar to the ones observed in experiments. In this case the field is effectively space charge limited at all voltages above 2 kV, and for these voltages the field is more or less constant after 10 µs. While these estimates do indicate that the field within the cyclohexane is indeed space charge limited, at least at higher voltages, they should not be used in further work as estimates for the field within cyclohexane at high voltages, because of the overall shortcomings for the model.

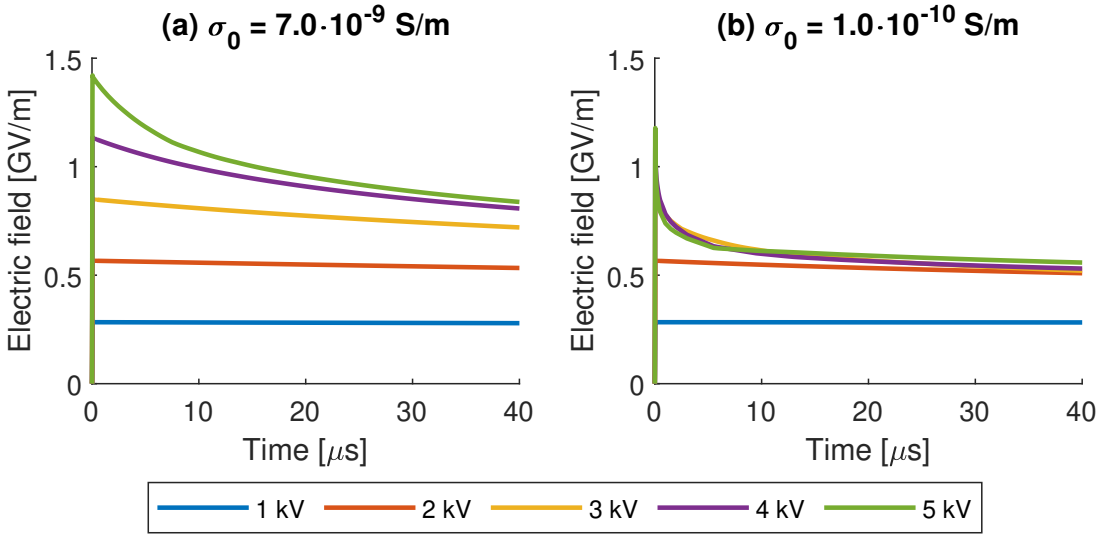

Figure 5.6: Electric field at the tip of the 2 µm needle electrode in numerical simulations with the conductivity given in Equation 4.3 (a) and 4.4 (b).

These results show that the conductivity of cyclohexane can not be explained by a simple simple exponentially field dependent conductivity. A more complex model is likely needed to adequately describe the behavior of cyclohexane at high voltage. It might be necessary to consider mechanisms such as ionization of cyclohexane, multiple charge carriers and hydrodynamic currents to accurately describe the phenomena taking place within the cyclohexane when the high voltage is applied. Because of the weak fit to the experimental data, it is not possible to determine which conduction mechanisms are dominant, and further work on this subject should be done on developing more complex models to describe the conduction mechanisms in cyclohexane.

Chapter 6

Conclusions

Currents through cyclohexane have successfully been measured using differential charge measurements with a needle-plane geometry. Measurements have been performed with two different needle electrodes, with 2 and 6 µm tip radius, and at both polarities. As high voltage pulses with short rise times are applied to the plane electrode, a relatively high current occurs, which slowly decreases until a steady current is reached from about 10 µs. This is consistent with the behavior associated with space charge limited fields. The measurements with the 6 µm needle electrode display lower currents than the 2 µm, because of the lower field at the tip of the needle, and the difference is particularly apparent for the steady current later in the pulse.

For the measurements with the 2 µm electrode, the space charge limited current was slightly higher when the plane electrode was at positive polarity, which is likely related to charge injection from the negative needle electrode. This behavior was not observed in the measurements with the 6 µm electrode, but the space charge limited currents were in this case even smaller, which makes it difficult to observe any clear trends.

The attempts at fitting a numerical model with a simple exponentially field dependent conductivity to the experimental results were not successful. While the model shows similar behavior to the real system, with a high initial current that gradually decreases to a steady current, it was found to either underestimate the initial current or overestimate the steady current, depending on the conductivity. Furthermore, the conductivity fitted to the results with the 2 µm electrode did not fit at all for the measurements with the 6 µm electrode. This indicates that the conductivity of cyclohexane can not be explained by a simple exponentially field dependent conductivity. A more complex model is likely required to accurately predict the behavior of the real system, and further work should be done to develop such a model.

Bibliography

[1] N. Mohan et al. "Teaching utility applications of power electronics in a first course on power systems". In: *IEEE Transactions on Power Systems* 19.1 (2004), pp. 40–47.

[2] J. Kassakian and T. Jahns. "Evolving and Emerging Applications of Power Electronics in Systems". In: *Emerging and Selected Topics in Power Electronics, IEEE Journal of* 1 (June 2013), pp. 47–58. DOI: 10.1109/JESTPE.2013.2271111.

[3] F. Blaabjerg, Zhe Chen, and S. B. Kjaer. "Power electronics as efficient interface in dispersed power generation systems". In: *IEEE Transactions on Power Electronics* 19.5 (2004), pp. 1184–1194.

[4] International Energy Agency. *Smart Grids*. 2011, p. 52. DOI: https://doi.org/10.1787/9789264115071-en.

[5] M. Ghassemi. "PD measurements, failure analysis, and control in high-power IGBT modules". In: *High voltage* 3.3 (2018), pp. 170–178.

[6] A. Cavallini. "Insulation degradation under fast, repetitive voltage pulses". In: *CIGRE 703* (2017).

[7] L. Dissado. *Electrical degradation and breakdown in polymers*. eng. Vol. vol. 9. IET materials and devices series. London: Institution of Engineering and Technology, 1992. ISBN: 9780863411960.

[8] L. Dumitrescu et al. "Study of streamer inception in cyclohexane with a sensitive charge measurement technique under impulse voltage". In: *Journal of Electrostatics* 53.2 (2001). Selected Papers of the International Workshop on Electrical Condu ction, Convection and Breakdown in Fluids, pp. 135–146. ISSN: 0304-3886. DOI: https://doi.org/10.1016/S0304-3886(01)00136-X.

[9] S. Boggs. "Very high field phenomena in dielectrics". In: *IEEE transactions on dielectrics and electrical insulation* 12.5 (2005), pp. 929–938.

[10] A. Denat, J. P. Gosse, and B. Gosse. "Electrical conduction of purified cyclohexane in a divergent electric field". In: *IEEE Transactions on Electrical Insulation* 23.4 (1988), pp. 545–554. DOI: 10.1109/14.7324.

[11] V. Adamec and J. H. Calderwood. "Electrical conduction in dielectrics at high fields". In: *Journal of Physics D: Applied Physics* 8.5 (Apr. 1975), pp. 551–560. DOI: 10.1088/0022-3727/8/5/015.

[12] H. J. Wintle. "Charge motion and trapping in insulators: surface and bulk effects". In: *IEEE Transactions on Dielectrics and Electrical Insulation* 6.1 (1999), pp. 1–10. DOI: 10.1109/94.752003.

[13] G. Teyssedre and C. Laurent. "Charge transport modeling in insulating polymers: from molecular to macroscopic scale". In: *IEEE Transactions on Dielectrics and Electrical Insulation* 12.5 (2005), pp. 857–875. DOI: 10.1109/TDEI.2005.1522182.

[14] Ø. Hestad, P.-O. Åstrand, and L. Lundgaard. "n-tridecane as a Model System for Polyethylene: Comparison of Pre-breakdown Phenomena in Liquid and Solid Phase Stressed by a Fast Transient". In: *Dielectrics and Electrical Insulation, IEEE Transactions on* 18 (Dec. 2011), pp. 1929–1946. DOI: 10.1109/TDEI.2011.6118631.

[15] H. Bærug. *Field Dependent Conductvitiy of Insulation Materials for Power Electronics (unpublished)*. Project report in TMT4500. Department of Materials Science & Engineering, NTNU – Norwegian University of Science & Technology, Dec. 2019.

[16] COMSOL. *COMSOL Cylopedia*. URL: https://www.comsol.com/multiphysics/ (visited on 02/20/2020).

[17] P. W. Gross and P. R. Kotiuga. *Electromagnetic Theory and Computation : A Topological Approach*. Mathematical Sciences Research Institute Publications Vol. 48. Cambridge University Press, 2004. ISBN: 9780521801607.

[18] T. Baumann et al. "Field-enhancing defects in polymeric insulators causing dielectric aging". In: *IEEE Transactions on Electrical Insulation* 24.6 (1989), pp. 1071–1076. DOI: 10.1109/14.46340.

[19] Ø. Hestad. *Prebreakdown phenomena in solids and liquids stressed by fast transients: The effect of additives and phase*. 2011.

[20] T. Top, G. Massala, and O. Lesaint. "Streamer propagation in mineral oil in semi-uniform geometry". In: *IEEE transactions on dielectrics and electrical insulation* 9.1 (2002), pp. 76–83.

[21] O. Hestad, L. Lundgaard, and D. Linhjell. "New experimental system for the study of the effect of temperature and liquid to solid transition on streamers in dielectric liquids: Application to cyclohexane". In: *IEEE Transactions on Dielectrics and Electrical Insulation* 17.3 (2010), pp. 764–774.

[22] O. Lesaint. "Prebreakdown phenomena in liquids: propagation 'modes' and basic physical properties". In: *Journal of Physics D: Applied Physics* 49.14 (2016), p. 144001.

[23] T. Lewis. "A new model for the primary process of electrical breakdown in liquids". In: *IEEE Transactions on Dielectrics and Electrical Insulation* 5.3 (1998), pp. 306–315.

[24] P. Gournay and O. Lesaint. "A study of the inception of positive streamers in cyclohexane and pentane". In: *Journal of Physics D: Applied Physics* 26.11 (1993), pp. 1966–1974. DOI: 10.1088/0022-3727/26/11/019.

[25] J.-M. Jin. *The finite element method in electromagnetics*. John Wiley & Sons, 2015.

[26] Merck. *Supelco Cyclohexane for analysis EMSURE®ACS, ISO, Reag. Ph Eur*. URL: https://www.merckmillipore.com/NO/en/product/Cyclohexane,MDA_CHEM-109666?bd=1#anchor_Product%20Information (visited on 05/07/2020).

[27] MATLAB. *version 9.6.0 (R2019a)*. Natick, Massachusetts: The MathWorks Inc., 2019. URL: https://se.mathworks.com/products/matlab.html.

[28] R. Sigmond. "Simple passive electrical filter for discharge diagnostics". In: *11th Symp. on Elemenray Pocesses and Chemical Reactions in Low Temperature Plasma*. 1998, p. 256.

[29] COMSOL. *COMSOL Multiphysics 5.4*. URL: https://www.comsol.com (visited on 09/01/2020).

[30] Tektronix U.K Limited. *TDS 520 & 540 Digitizing Oscilloscopes, User Manual*. URL: https://www.tek.com/oscilloscope/tds540-manual/tds-520-540-digitizing-oscilloscopes-user-manual (visited on 09/07/2020).

[31] The Norwegian Communications Authority (Nkom). *Tillatelse til å bruke frekvenser*. URL: https://www.nkom.no/frekvenser-og-elektronisk-utstyr/tillatelse-til-a-bruke-frekvenser (visited on 09/07/2020).

[32] T. M. Aminabhavi et al. "Density, Viscosity, and Refractive Index of the Binary Mixtures of Cyclohexane with Hexane, Heptane, Octane, Nonane, and Decane at (298.15, 303.15, and 308.15) K". In: *Journal of Chemical & Engineering Data* 41.3 (1996), pp. 521–525. DOI: 10.1021/je950279c.

Appendix A

MATLAB code for investigating shape of needle electrodes

The following MATLAB code was developed to compare the shape of the different needle electrodes. First a x-axis is defined along the longitudinal axis of the needle, with $x = 0$ at the tip. Points are then manually selected on the surface of the needle, and are exported as csv-files for post-processing.

```
function curve_fitter()
close all; clear; clc;

n = 20; %number of points recorded for each side of the needle
scaleLength = 2; %length of the scale bar [um]
I = imread('N2_pre_A.tif'); %open image of needle
figure(1)
imshow(I)
hold on

%define x-axis along the center of the needle
%Click 1:select tip of the needle,
%Click 2/3: a point on either side of the needle near the base
disp('Enter x-axis');
xaxisInput = ginput(3);
xaxis = [xaxisInput(1,:) ; mean(xaxisInput(2:3,:),1)];
plot(xaxis(:,1), xaxis(:,2));
%plot a yaxis normal to the xaxis
yaxis = [xaxis(1,1), xaxis(1,2); xaxis(1,1) + xaxis(2,2) -
   xaxis(1,2), xaxis(1,2) + xaxis(1,1) - xaxis(2,1)];
plot(yaxis(:,1), yaxis(:,2));
```

```
21
22 %Click each side of the scale bar
23 disp('Enter scale');
24 scaleM = ginput(2);
25 distance = sqrt((scaleM(2,1)-scaleM(1,1))^2+(scaleM(2,2)-scaleM
     (1,2))^2);
26 scale = scaleLength*10^(-6)/distance; %m
27
28 disp('Enter points on left side, start from tip');
29 lPoints = ginput(n);
30 scatter(lPoints(:,1), lPoints(:,2));
31 lPointsOut = zeros(n, 2); %pre-allocate
32 disp('Enter points on right side, start from tip');
33 rPoints = ginput(n);
34 scatter(rPoints(:,1), rPoints(:,2));
35 rPointsOut = zeros(n, 2); %pre-allocate
36
37 %calculate x and y coordinates for each of the points
38 for i = 1:length(lPoints)
39     lPointsOut(i,2) = ptl(lPoints(i,:),yaxis(1,:),yaxis(2,:));
40     lPointsOut(i,1) = ptl(lPoints(i,:),xaxis(1,:),xaxis(2,:));
41     rPointsOut(i,2) = ptl(rPoints(i,:),yaxis(1,:),yaxis(2,:));
42     rPointsOut(i,1) = ptl(rPoints(i,:),xaxis(1,:),xaxis(2,:));
43 end %for
44 %save coordinates in csv files for post-processing [m]
45 csvwrite('points_right.csv', rPointsOut*scale);
46 csvwrite('points_left.csv', lPointsOut*scale);
47 end %func
48
49 function d = ptl(pt, v1, v2) %function to find distance between
       points and axis
50     v1=v1(:)';%force 1x3 or 1x2
51     if length(v1)==2,v1(3)=0;end
52     v2=v2(:)';%force 1x3 or 1x2
53     if length(v2)==2,v2(3)=0;end
54     if size(pt,2)==2,pt(1,3)=0;end
55     v1_ = repmat(v1,size(pt,1),1);
56     v2_ = repmat(v2,size(pt,1),1);
57     a = v1_ - v2_;
58     b = pt - v2_;
59     d = sqrt(sum(cross(a,b,2).^2,2)) ./ sqrt(sum(a.^2,2));
60 end %func point to line
```

Appendix B

MATLAB code for parameter study

This MATLAB code was developed to run the COMSOL model with a wide range of different parameter values. The input file is an Excel-document with three sheets: 'parameters', 'variables' and 'studies'. The first column of each sheet contains the name of the parameter (defined in the model), and the following columns contains the values for the given parameter. Each of the sheets defines:

- Parameters: Parameters that are constant for all the studies performed
- Variables: The model will be run with all possible combinations of the variables defined in this sheet.
- Studies: Parameters for the studies which are run. Contains time steps for the studies as well as the dataset-tag where COMSOL stores the results

The resulting charge, maximum field and maximum conductivity, at each time step is saved as mat-files for post-processing.

```
function parameter_study()
clc; clear; close all;

model = mphopen('FastTrans_Conductivity.mph'); %Load model
inputs = {'inputs_2um_n1.xlsx'}; %Input file(s)

for input=1:length(inputs)
    fprintf('Start input %i', input);
    data = struct; %Define output file
    %LOAD INPUTS FROM EXCEL FILE WITH MULTIPLE SHEETS
    params = table2array(readtable(inputs{input},'Sheet','
       parameters')); %Static parameters
```

```
12      vars = table2array(readtable(inputs{input},'Sheet','
           variables')); %Variable parameters
13      studies = table2cell(readtable(inputs{input},'Sheet','
           studies')); %Settings for the Comsol study
14      %SET PARAMETERS
15      [rowPar, ~] = size(params);
16      for i = 1:rowPar %Set constant parameters from excel file
17          model.param.set(params{i,1},params{i,2});
18      end %for i
19      %GET ALL COMBINATIONS OF VARIABLES
20      [varNum, ~] = size(vars); %Number of variables
21      %Prepare input for allcomb function:
22      varSplit= cell(1, varNum); %Each cell is input variable
23      for i = 1:varNum %remove expressions and empty cells
24          vari = vars(i,2:end);
25          varSplit(i) = {vari(~cellfun('isempty', vari))};
26      end %for i
27      combinations = allcomb(varSplit{:}); %Combinations of vars
28      [combNum, ~] = size(combinations); %Number of combinations
29      fprintf('\nNumber of combinations: %i\n', combNum);
30      %SET STUDY TIME STEPS AND PRE-ALLOCATION
31      for i= 1:length(studies(:,1))
32          model.param.set(sprintf('std%i_t0', studies{i,1}),
               studies{i,2});
33          model.param.set(sprintf('std%i_dt', studies{i,1}),
               studies{i,3});
34          model.param.set(sprintf('std%i_tstop', studies{i,1}),
               studies{i,4});
35          %Create time vector;
36          stdStr = sprintf('std%i',studies{i,1}); %Fieldname
37          t0 = studies{1,2};
38          t0 = str2double(t0(1:end-4))*10^(-9);
39          trise = (0:1E-9:t0);
40          trest = (model.param.evaluate(sprintf('%s_t0',stdStr)):
               model.param.evaluate(sprintf('%s_dt',stdStr)):model.
               param.evaluate(sprintf('%s_tstop',stdStr)));
41          data.(stdStr).t = [trise, trest];
42          L = length(data.(stdStr).t);
43          %Pre-allocate;
44          data.(stdStr).Emax = zeros(combNum, L);
45          data.(stdStr).condMax = zeros(combNum, L);
46          data.(stdStr).charge = zeros(combNum, L);
47      end %for i
```

```
    for i=1:combNum %cycle through variable combinations
        fprintf('\nCombination %i\n', i);
        tic;
        for k=1:varNum %set variable parameters
            model.param.set(vars{k,1},combinations{i,k});
        end %for k

        for k = 1:length(studies(:,1))
            model.geom.run;
            model.mesh.run;
            model.study(sprintf('std%i',studies{k,1})).run;
            dset = studies{k,5};
            stdStr = sprintf('std%i',studies{k,1}); %fieldname
            data.(stdStr).Emax(i,:) = mphglobal(model, 'E_max',
                'dataset', dset, 'unit', 'GV/m').';
            data.(stdStr).condMax(i,:) = mphglobal(model, '
               cond_max', 'dataset', dset, 'unit', 'S/m').';
            data.(stdStr).charge(i,:) = mphglobal(model, '
               ind_charge', 'dataset', dset, 'unit', 'pC').';
        end %for k
        toc %display combination time
    end %for i
    combinations = cell2table(combinations, 'VariableNames',
       vars(:,1), 'RowNames', cellstr(string(1:combNum)));
    save(sprintf('output%i.mat',input),'combinations','data');
    fprintf('\nSaved %s \n', sprintf('output%i.mat',input));
    clearvars -except input inputs model %reduce memory use
end %for INPUT
end %func

%% ALLCOMB FUNC [Created by Jos (10584), MATLAB Central File
   Exchange, Retrieved July 22 2019]

function A = allcomb(varargin) %Gives a matrix with all
   possible combinations of varargin
narginchk(1,Inf) ;
NC = nargin ;
% check if we should flip the order
if ischar(varargin{end}) && (strcmpi(varargin{end}, 'matlab')
   || strcmpi(varargin{end}, 'john'))
    NC = NC-1 ;
    ii = 1:NC ; % now first argument will change fastest
else
```

```
84      % default: enter arguments backwards
85      ii = NC:-1:1 ;
86  end
87  args = varargin(1:NC) ;
88  if any(cellfun('isempty', args)) % check for empty inputs
89      warning('ALLCOMB:EmptyInput','EMPTY INPUT.') ;
90      A = zeros(0, NC) ;
91  elseif NC == 0 % no inputs
92      A = zeros(0,0) ;
93  elseif NC == 1 % a single input, nothing to combine
94      A = args{1}(:) ;
95  else
96      isCellInput = cellfun(@iscell, args) ;
97      if any(isCellInput)
98          if ~all(isCellInput)
99              error('ERROR') ;
100         end
101         % for cell input, indices to get all combinations
102         ix = cellfun(@(c) 1:numel(c), args, 'un', 0) ;
103         % flip using ii if last column is changing fastest
104         [ix{ii}] = ndgrid(ix{ii}) ;
105         A = cell(numel(ix{1}), NC) ; % pre-allocate the output
106         for k = 1:NC %combine
107             A(:,k) = reshape(args{k}(ix{k}), [], 1) ;
108         end
109     else
110         % non-cell input
111         % flip using ii if last column is changing fastest
112         [A{ii}] = ndgrid(args{ii}) ;
113         % concatenate
114         A = reshape(cat(NC+1,A{:}), [], NC) ;
115     end
116 end %if
117 end %func
```

Appendix C

Measurements with 2 µm needle and positive plane electrode

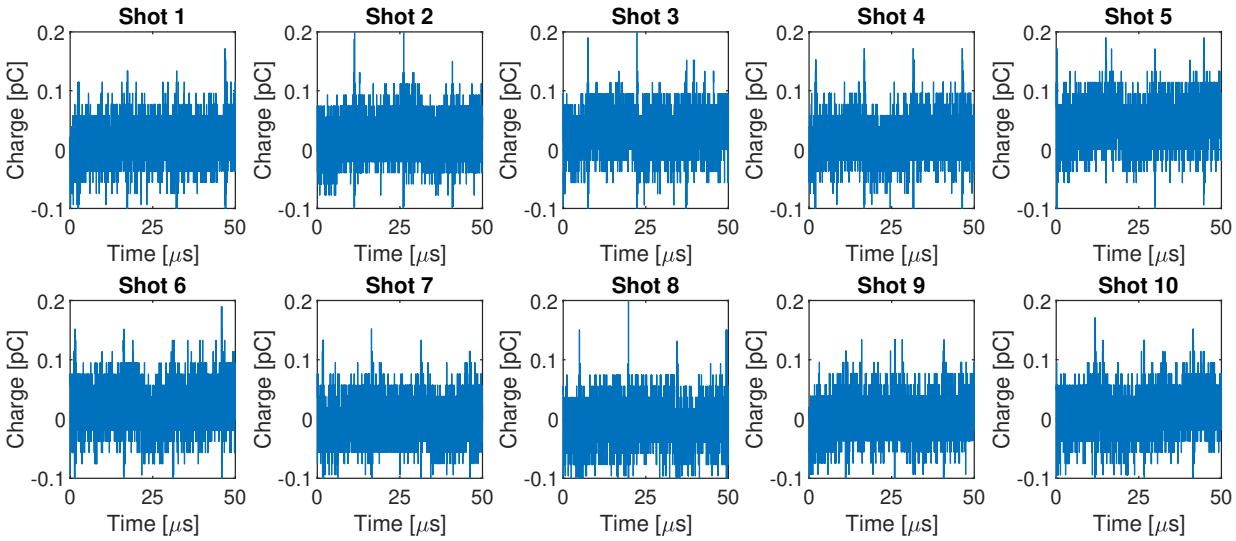

Figure C.1: Charge measurements with 2 µm electrode and positive plane electrode at 1 kV

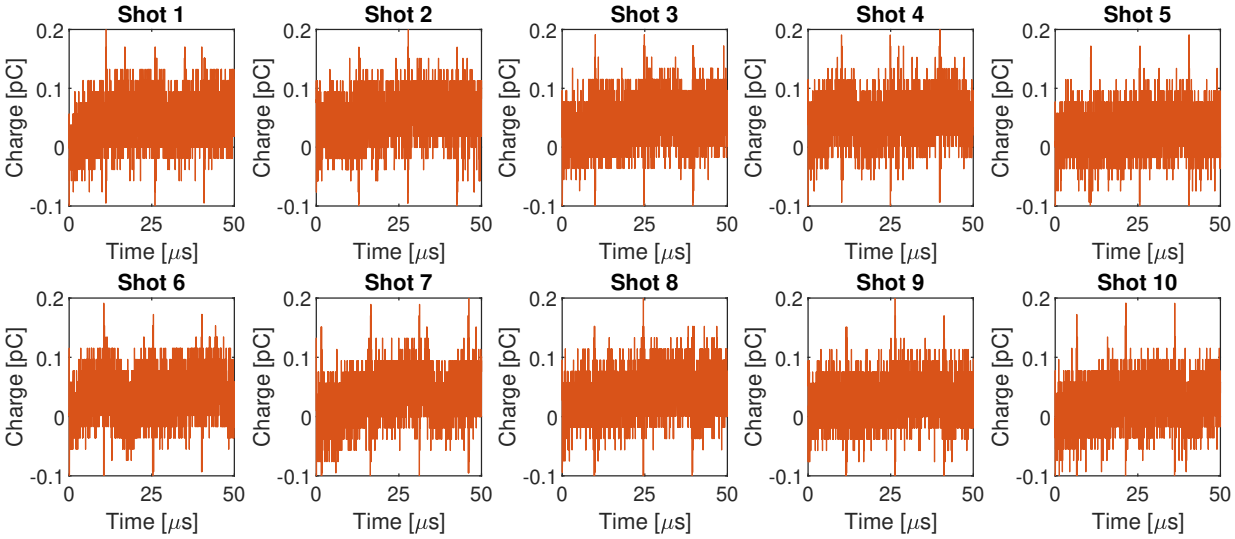

Figure C.2: Charge measurements with 2 µm electrode and positive plane electrode at 2 kV

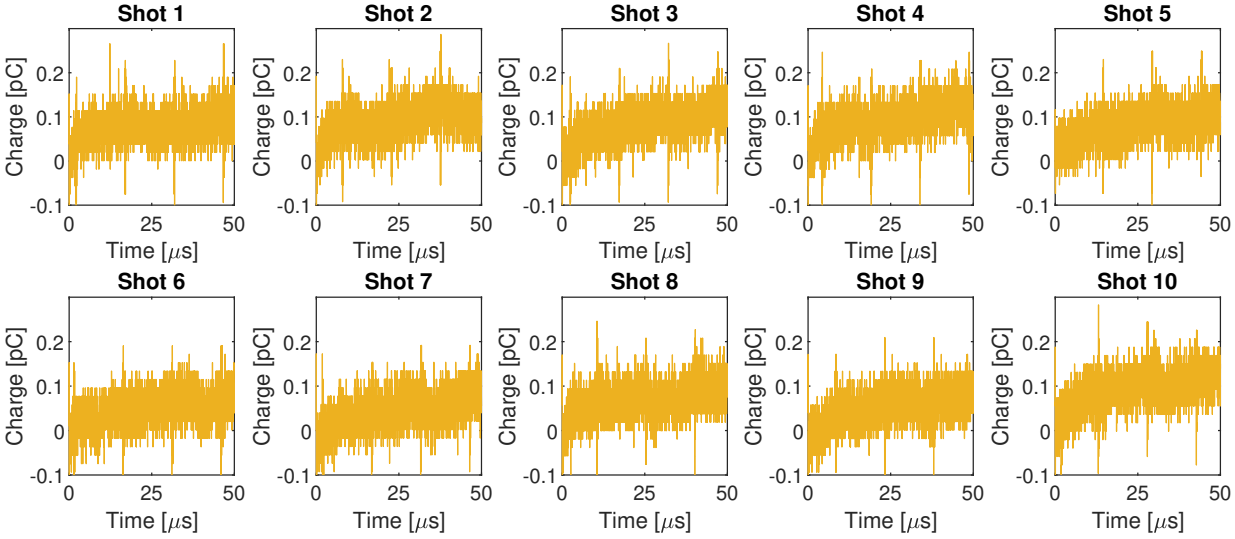

Figure C.3: Charge measurements with 2 µm electrode and positive plane electrode at 3 kV

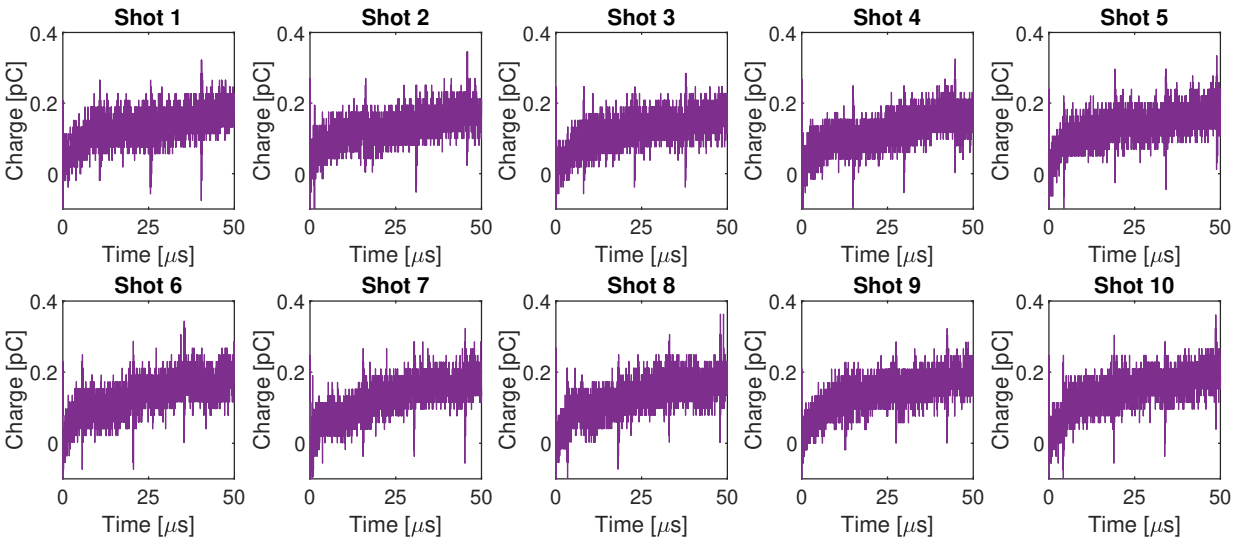

Figure C.4: Charge measurements with 2 µm electrode and positive plane electrode at 4 kV

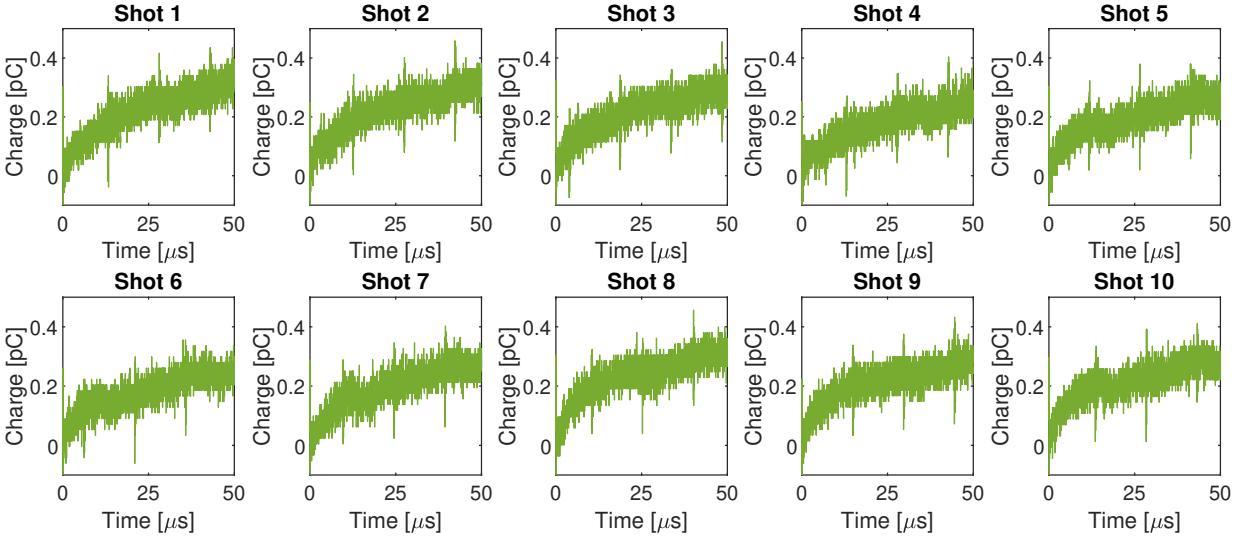

Figure C.5: Charge measurements with 2 µm electrode and positive plane electrode at 5 kV

Appendix D

Measurements with 2 µm needle and negative plane electrode

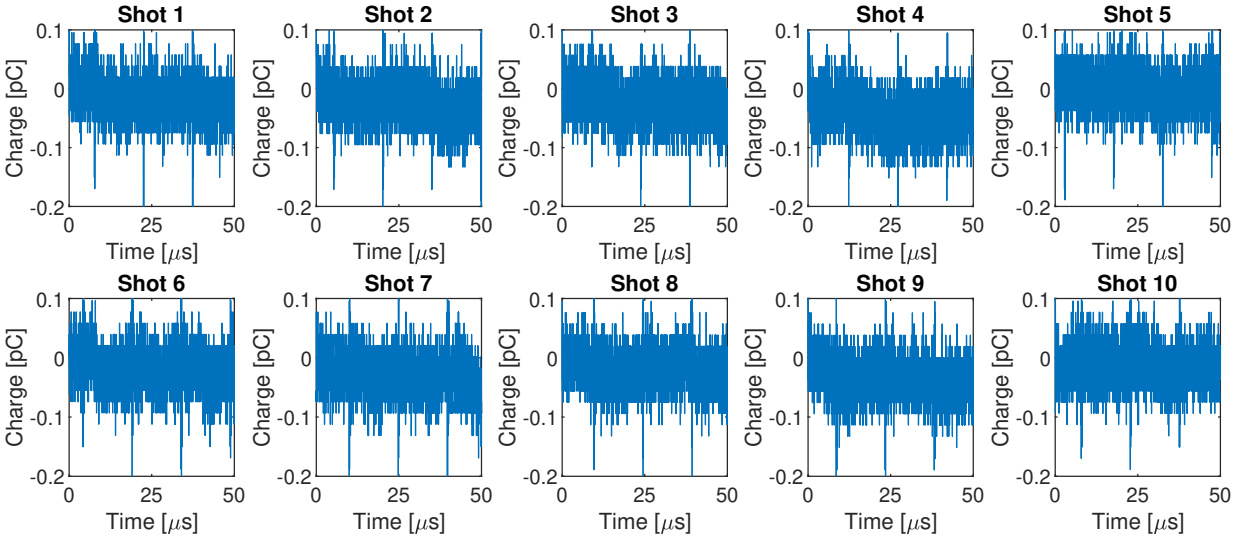

Figure D.1: Charge measurements with 2 µm electrode and negative plane electrode at 1 kV

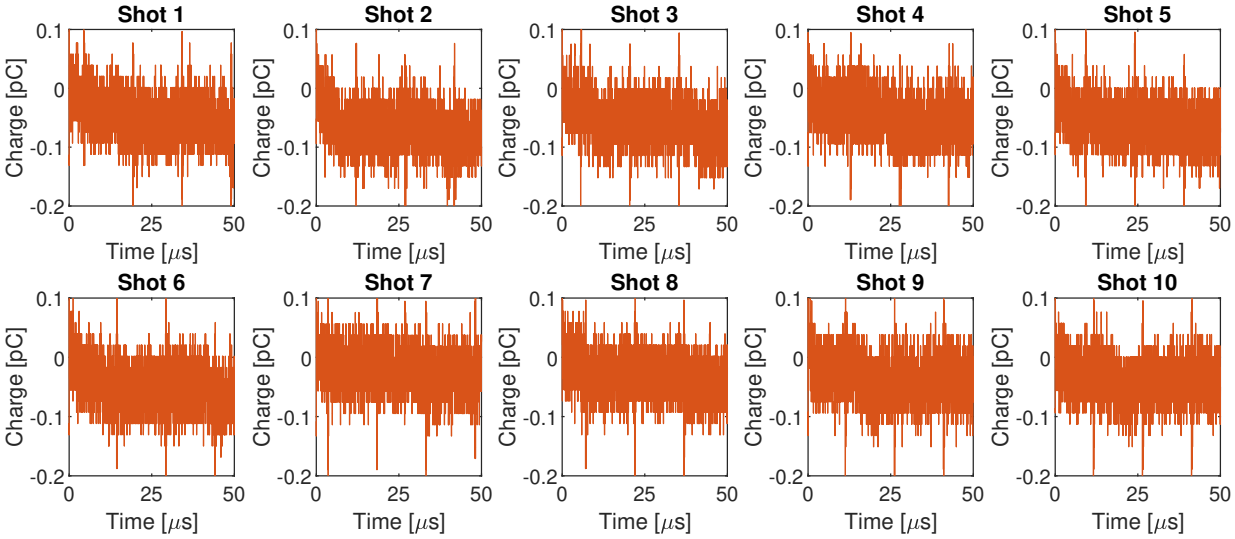

Figure D.2: Charge measurements with 2 µm electrode and negative plane electrode at 2 kV

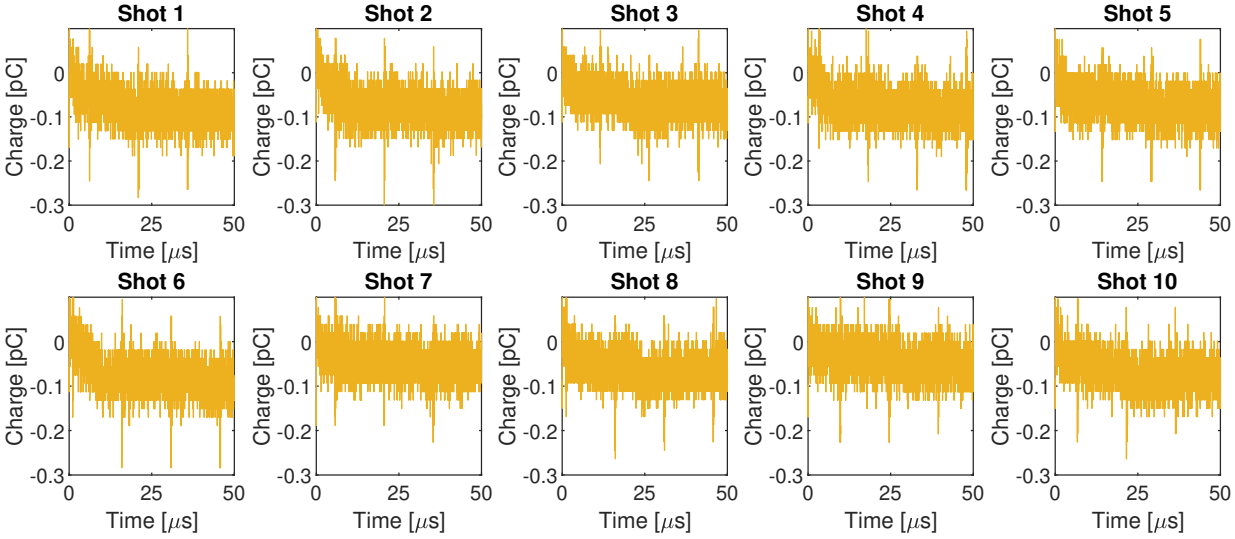

Figure D.3: Charge measurements with 2 µm electrode and negative plane electrode at 3 kV

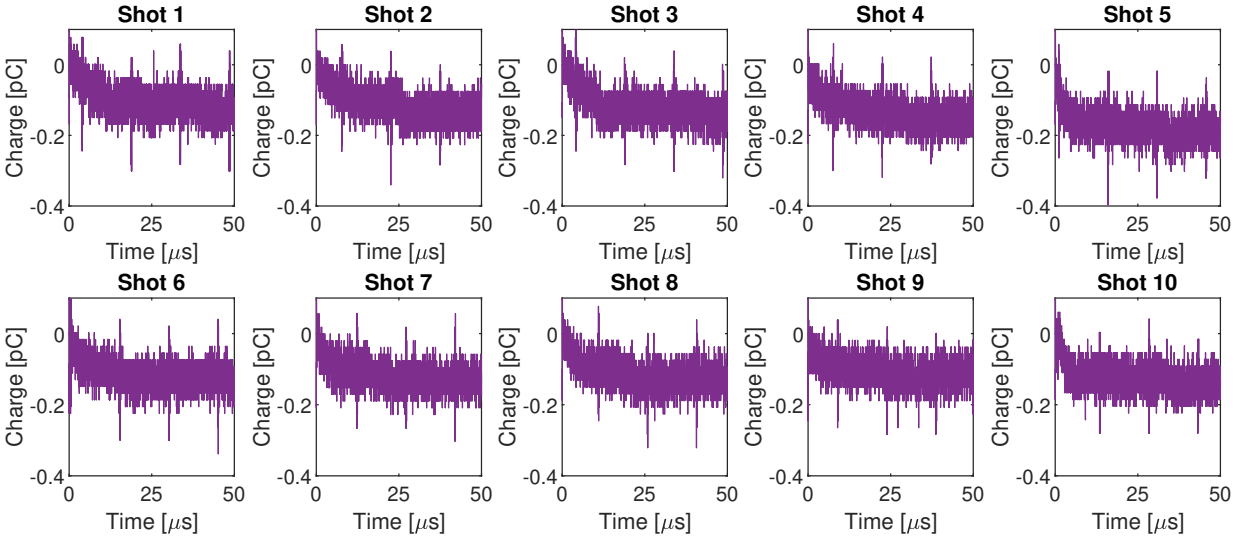

Figure D.4: Charge measurements with 2 µm electrode and negative plane electrode at 4 kV

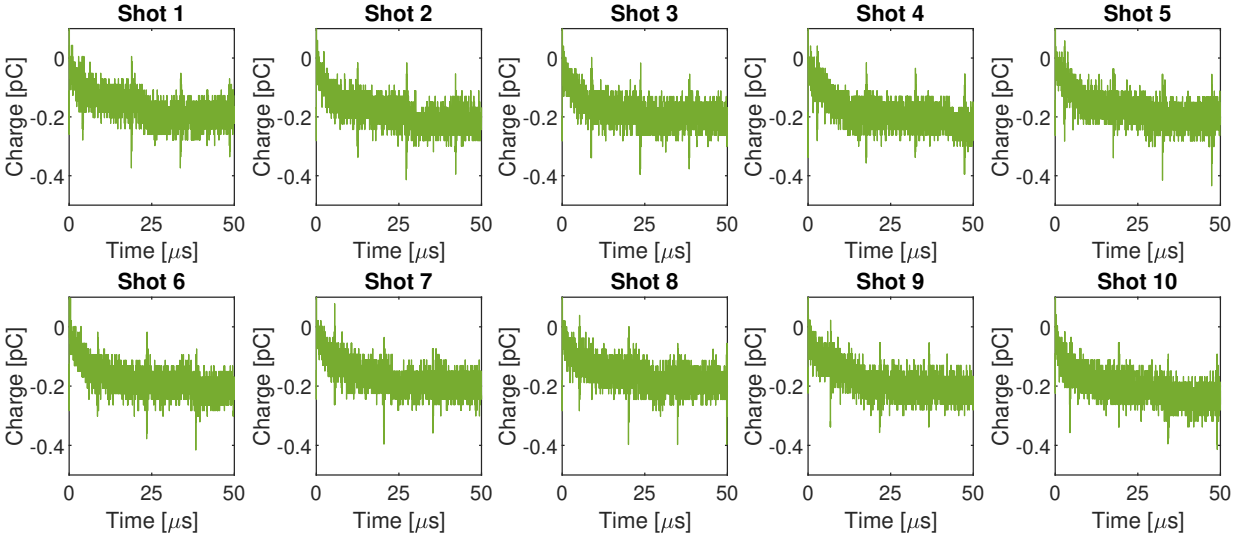

Figure D.5: Charge measurements with 2 µm electrode and negative plane electrode at 5 kV

Appendix E

Measurements with 6 µm needle and positive plane electrode

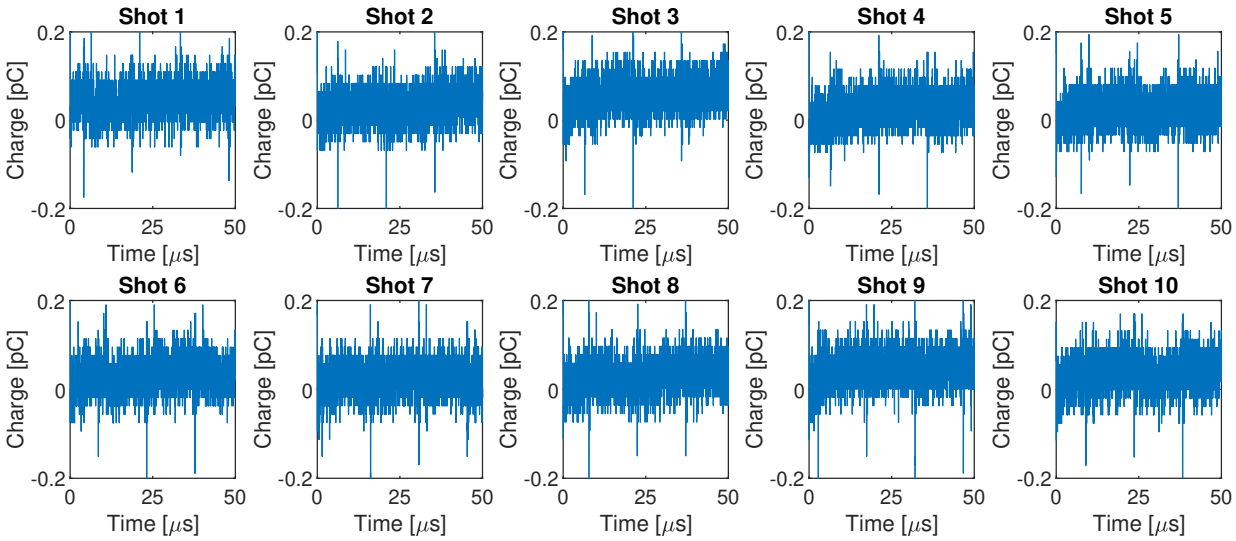

Figure E.1: Charge measurements with 6 µm electrode and positive plane electrode at 2 kV

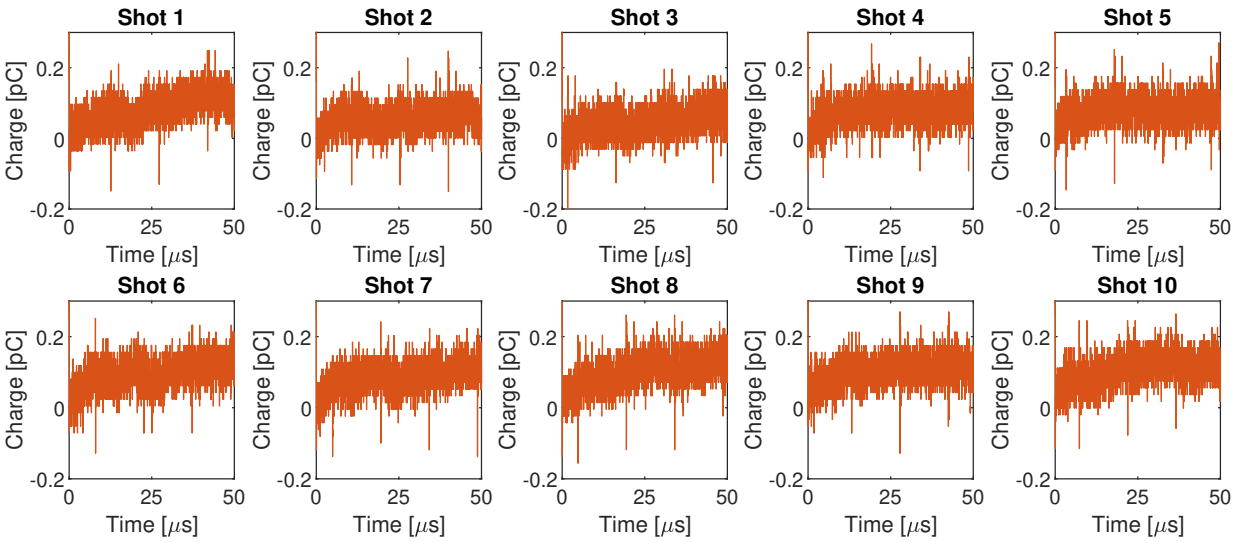

Figure E.2: Charge measurements with 6 µm electrode and positive plane electrode at 4 kV

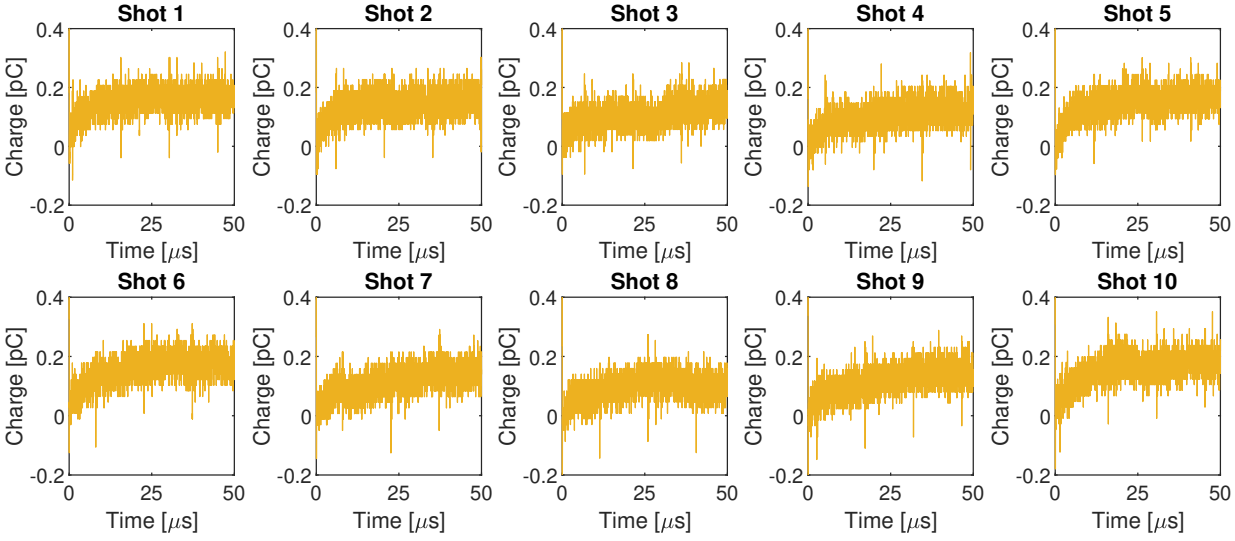

Figure E.3: Charge measurements with 6 µm electrode and positive plane electrode at 6 kV

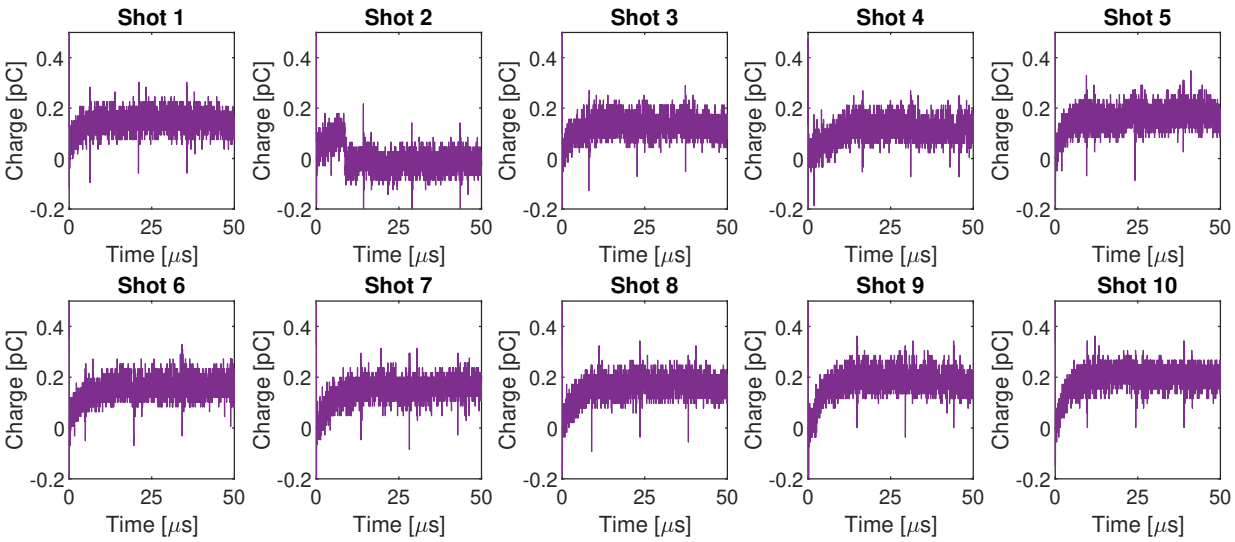

Figure E.4: Charge measurements with 6 µm electrode and positive plane electrode at 8 kV

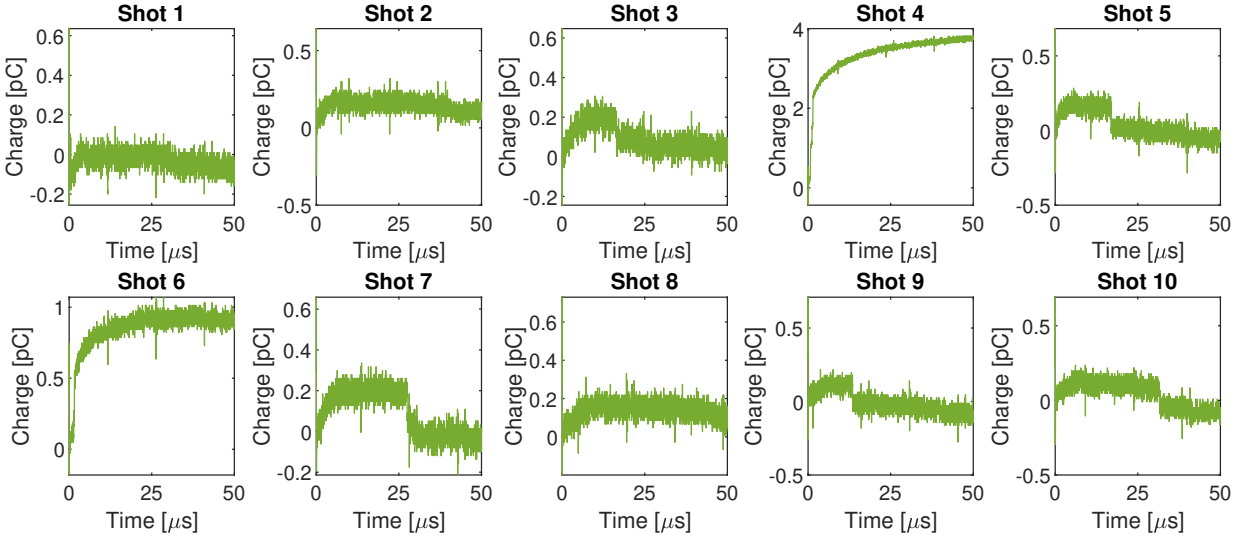

Figure E.5: Charge measurements with 6 µm electrode and positive plane electrode at 10 kV

Appendix F

Measurements with 6 µm needle and negative plane electrode

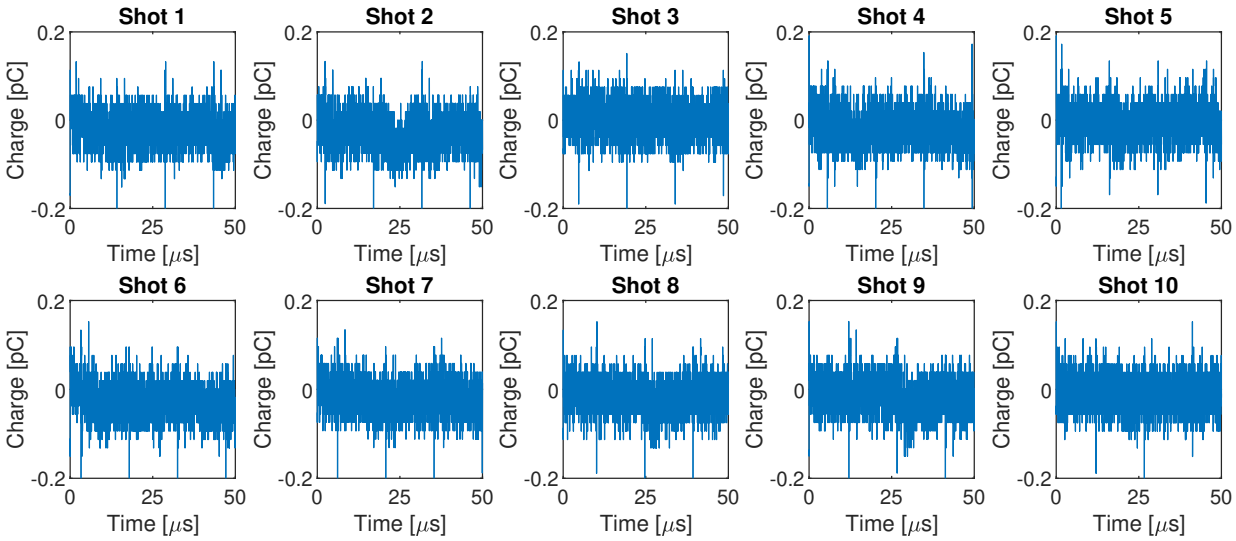

Figure F.1: Charge measurements with 6 µm electrode and negative plane electrode at 2 kV

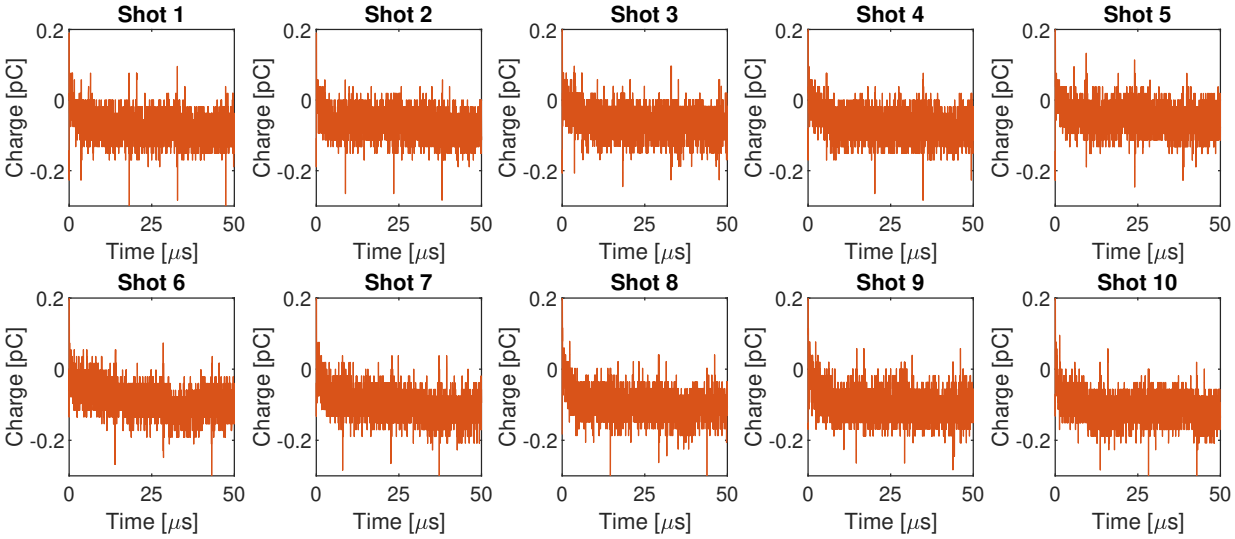

Figure F.2: Charge measurements with 6 µm electrode and negative plane electrode at 4 kV

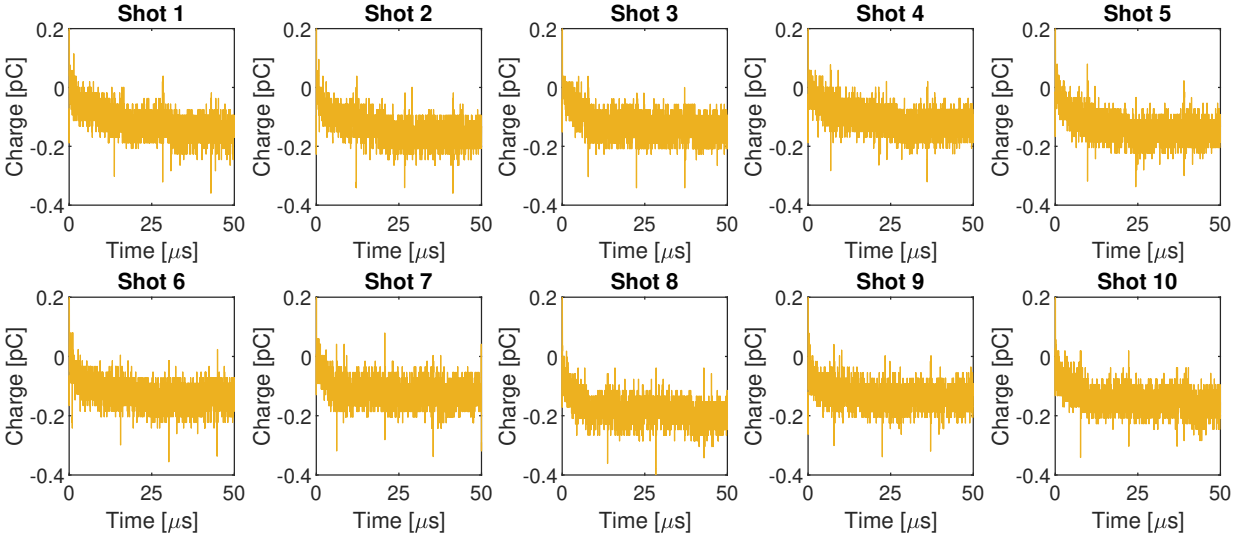

Figure F.3: Charge measurements with 6 µm electrode and negative plane electrode at 6 kV

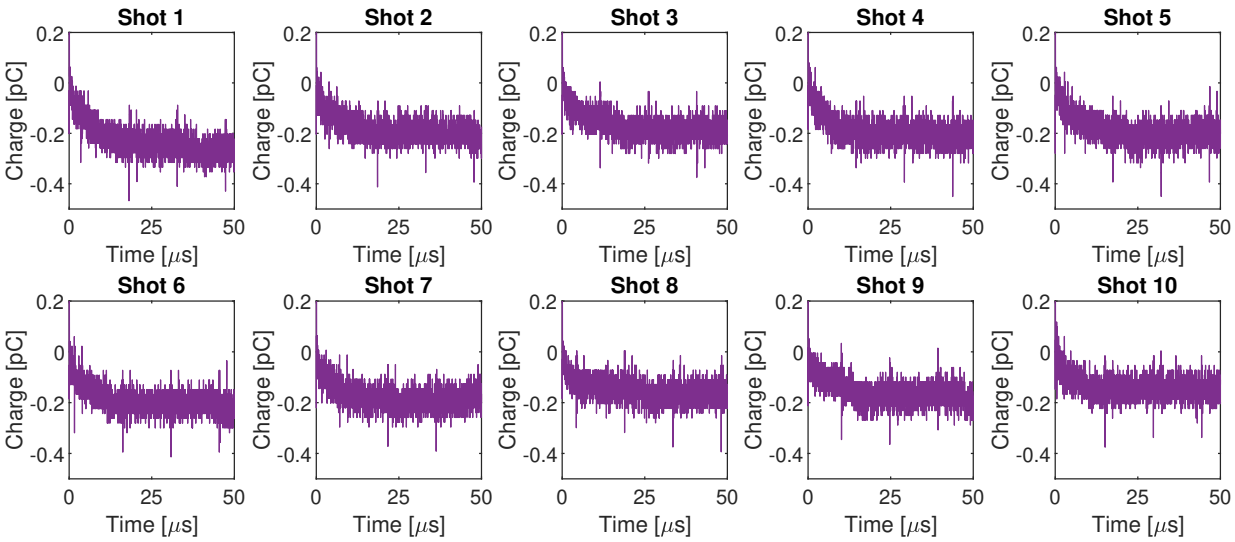

Figure F.4: Charge measurements with 6 µm electrode and negative plane electrode at 8 kV

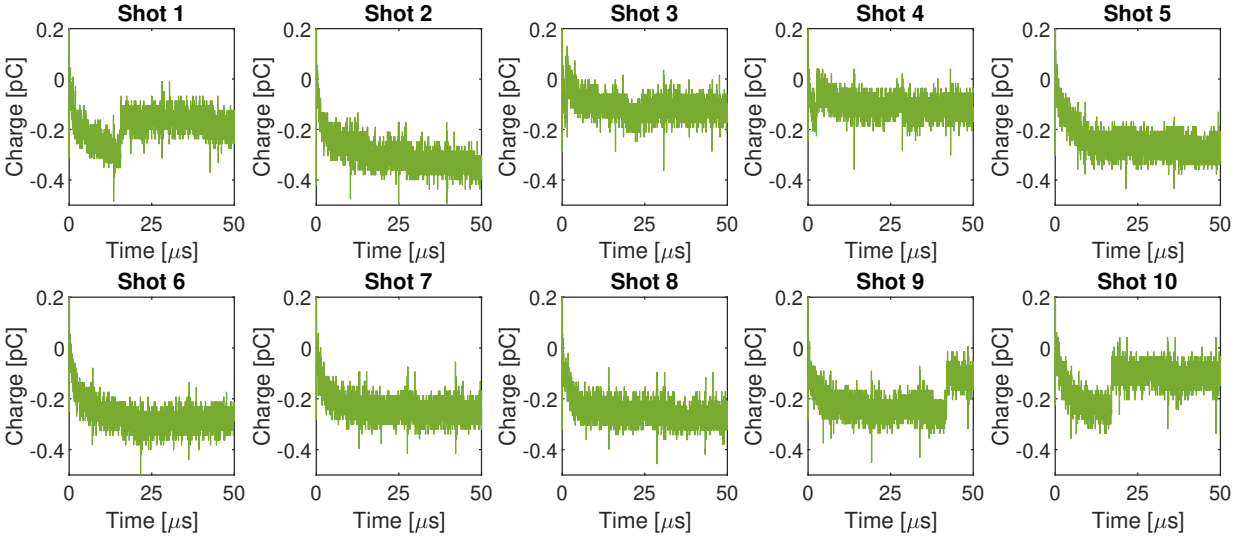

Figure F.5: Charge measurements with 6 µm electrode and negative plane electrode at 10 kV

NTNU

Norwegian University of
Science and Technology